Computational issues in gradient plasticity

6

Computational Issues in Gradient Plasticity

R. de Borst[1], J. Pamin and L.J. Sluys

Delft University of Technology, Faculty of Civil Engineering,

6.1 INTRODUCTION

Failure in cohesive-frictional and quasi-brittle materials involves localization of deformation, i.e. we observe that at incipient failure small zones of highly strained material develop rather abruptly, while the remainder of the structure experiences almost no additional straining. Examples are cracks in concrete, shear bands in soils and metals, dilatational bands in polymers and rock faults. Experiments show that these localization phenomena are accompanied by a more or less sharp decrease of the load-carrying capacity. This phenomenon is commonly named strain softening and can lead to ill-posed boundary value problems in standard continuum theories, since in quasi-static problems ellipticity of the governing set of differential equations is no longer assured, while in dynamic problems hyperbolicity can be lost at least in certain parts of the body. In numerical simulations we observe an extreme mesh sensitivity in terms of fineness and direction of the grid lines. To remedy this improper behaviour the standard continuum model must be enriched. Here, various strategies are possible, such as nonlocal approaches, micro-polar continua, rate-dependent approaches and continuum models enhanced with higher-order deformation gradients. Most of these approaches are discussed at length in the other chapters of this volume, and the physical motivations for the various enrichments are laid out in detail. In this chapter, we shall concentrate on the implications of using higher-order continuum models in large-scale numerical simulations of localization and failure. In particular, we consider one such continuum model,

1. Also at Eindhoven University of Technology, Faculty of Mechanical Engineering.

Continuum Models for Materials with Microstructure. Edited by H.-B. Mühlhaus

namely a gradient plasticity model, and we shall demonstrate how effective numerical strategies for this enhanced continuum model can be developed.

This chapter is laid out as follows. First, the essentials of gradient plasticity are outlined. A weak format of the governing partial differentials is given, which is amenable to a finite element formulation. Next, two such formulations are given, whereby particular attention is given to the continuity requirements that are imposed by the presence of higher-order deformation gradients. Also, difficulties are discussed that relate to the integration of the rate equations in gradient plasticity. Subsequently, a number of finite elements are formulated and assessed in numerical simulations of shear banding in softening, non-associated plasticity. Finally, issues are discussed regarding the spatial and temporal discretization in gradient-plasticity under dynamic loading conditions. The pivotal role of dispersion in setting the band width in enriched continuum models is emphasized.

6.2 GRADIENT PLASTICITY

6.2.1 Essentials

Gradient dependence has first been used within the theory of rigid-plastic materials for the analysis of persistent slip bands [1-3] and shear bands in metals [4]. The second derivative of an accumulated shear strain $\bar{\gamma}$ was included in the shear stress-strain rate equation [4] following the argument of the material frame indifference:

$$\tau = \left[\bar{\tau}(\bar{\gamma}) - c \frac{\mathrm{d}^2 \bar{\gamma}}{\mathrm{d}x^2} \right] \frac{\dot{\gamma}}{|\dot{\gamma}|} , \tag{6.1}$$

with τ the shear stress, $\dot{\gamma}$ the shear strain rate, $\bar{\tau}(\bar{\gamma})$ the yield stress and c a positive phenomenological constant. This approach was used as a localization limiter by Lasry and Belytschko [5] and the constitutive law has been written in a uniaxial case as follows:

$$\sigma = E_t \left[\varepsilon + \alpha \frac{\mathrm{d}^2 \varepsilon}{\mathrm{d}x^2} \right] , \tag{6.2}$$

with E_t the tangent modulus and α a gradient constant.

In a more general approach the Laplacian of an effective deformation measure γ has been included in the yield condition [6]

$$\tau = \bar{\tau}(\gamma) - c\nabla^2 \gamma , \quad c > 0 , \tag{6.3}$$

where τ is the second invariant of the deviatoric stress tensor and $\bar{\tau}(\gamma)$ is the hardening law. Gradients of higher order have been introduced in the yield function in [6,7]. The dependence of the hardening law on the first-order gradient of an inelastic strain invariant has also been examined [8]. However, it was noted in [7] that when isotropy is assumed only even-order gradients are relevant.

For the analysis of shear bands in granular materials the gradient dependence has been postulated in both the flow rule [9]:

$$\dot{\varepsilon}^p = \beta(\gamma^p)\dot{\gamma}^p - d\nabla^2\dot{\gamma}^p \,, \quad d>0 \,, \tag{6.4}$$

in which $\dot{\varepsilon}^p$ is the volumetric plastic strain rate, $\dot{\gamma}^p$ is the plastic shear strain rate and β is the dilatancy coefficient, and in the Coulomb yield condition:

$$\tau/p = \mu(\gamma^p) - c\nabla^2\gamma^p \,, \quad c>0 \,, \tag{6.5}$$

where p is the mean pressure and μ is the friction coefficient. The modified flow rule and yield condition are coupled [9] and the constants d and c are related to a unique internal length, which can be associated with the grain size.

In this chapter we make use of a gradient-dependent plasticity theory [7,10], in which the yield condition is similar to eq. (6.3):

$$\phi(\boldsymbol{\sigma}) = \bar{\sigma}(\kappa) - \bar{c}\nabla^2\kappa \,, \tag{6.6}$$

where $\phi(\boldsymbol{\sigma})$ is an equivalent stress, κ is an invariant plastic strain measure, $\bar{\sigma}$ is the yield strength and $\bar{c}$ is a positive coefficient with the dimension of force. It is emphasized that the gradient terms disappear from the constitutive equations if a homogeneous state of strain and stress is analyzed. In this sense they can be treated as a singular perturbation of the standard equations. The gradient terms are negligible if strains vary slowly in space, but have a significant influence in presence of strain localization.

6.2.2 Incremental boundary value problem

For the formulation of the incremental boundary value problem in gradient plasticity [10] we introduce the displacement vector $\mathbf{u}=(u_x, u_y, u_z)$, the strain tensor in a vector form $\boldsymbol{\varepsilon}=(\varepsilon_{xx}, \varepsilon_{yy}, \varepsilon_{zz}, \gamma_{xy}, \gamma_{yz}, \gamma_{zx})$ and the stress tensor in a vector form $\boldsymbol{\sigma}=(\sigma_{xx}, \sigma_{yy}, \sigma_{zz}, \sigma_{xy}, \sigma_{yz}, \sigma_{zx})$. Under the assumption of small deformations and static loading we have the following equations for an elasto-plastic body occupying a volume V (Figure 6.1):

$$\mathbf{L}^T\boldsymbol{\sigma} + \mathbf{b} = \mathbf{0} \,, \tag{6.7}$$

$$\boldsymbol{\varepsilon} = \mathbf{L}\mathbf{u} \,, \tag{6.8}$$

$$\mathrm{d}\boldsymbol{\sigma} = \mathbf{D}^e(\mathrm{d}\boldsymbol{\varepsilon} - \mathrm{d}\lambda\mathbf{m}) \,, \tag{6.9}$$

where the d-symbol denotes a small increment and the superscript T is the transpose symbol. $\mathbf{L}$ is a differential operator matrix:

$$\mathbf{L}^T = \begin{bmatrix} \dfrac{\partial\cdot}{\partial x} & 0 & 0 & \dfrac{\partial\cdot}{\partial y} & 0 & \dfrac{\partial\cdot}{\partial z} \\ 0 & \dfrac{\partial\cdot}{\partial y} & 0 & \dfrac{\partial\cdot}{\partial x} & \dfrac{\partial\cdot}{\partial z} & 0 \\ 0 & 0 & \dfrac{\partial\cdot}{\partial z} & 0 & \dfrac{\partial\cdot}{\partial y} & \dfrac{\partial\cdot}{\partial x} \end{bmatrix} , \tag{6.10}$$

$\mathbf{b}$ is a body-force vector and $\mathbf{D}^e$ is the elastic stiffness matrix. Eq. (6.9) contains the

definition of the plastic strain increment vector:

$$\mathrm{d}\boldsymbol{\varepsilon}^{\mathrm{p}} = \mathrm{d}\lambda \mathbf{m} \,, \tag{6.11}$$

in which $\mathrm{d}\lambda$ is a plastic multiplier and $\mathbf{m}$ a vector, which defines the direction of the plastic flow. The gradient dependence is included solely in the definition of the yield function F

$$F = F(\sigma, \kappa, \nabla^2 \kappa) \,, \tag{6.12}$$

in which κ is the invariant plastic strain measure introduced before (the hardening parameter). Together with eqs (6.7)-(6.9) the Kuhn-Tucker conditions

$$\mathrm{d}\lambda \geq 0 \,, \quad F \leq 0 \,, \quad F\mathrm{d}\lambda = 0 \tag{6.13}$$

must be fulfilled. To complete the incremental boundary value problem we specify the standard static and kinematic boundary conditions on complementary parts of the body surface S:

$$\boldsymbol{\Sigma} \boldsymbol{\nu}_{\mathrm{s}} = \mathbf{t} \,, \quad \mathbf{u} = \mathbf{u}_{\mathrm{s}} \,, \tag{6.14}$$

where $\boldsymbol{\Sigma}$ is the stress tensor in a matrix form, $\boldsymbol{\nu}_{\mathrm{s}}$ denotes the outward normal to the surface S and $\mathbf{t}$ is the boundary traction vector.

Henceforth we shall consider the case of isotropic hardening/softening and gradient dependence, so that, in view of eq. (6.6), the yield function can be written as

$$F = \phi(\sigma) - \bar{\sigma}(\kappa) + \bar{c}\nabla^2 \kappa \,. \tag{6.15}$$

In general the hardening parameter κ can be a function of plastic strains and stresses. For algorithmic convenience we limit our discussion to the strain-hardening hypothesis,

$$\mathrm{d}\kappa = \sqrt{2/3 (\mathrm{d}\boldsymbol{\varepsilon}^{\mathrm{p}})^{\mathrm{T}} \mathbf{Q} \mathrm{d}\boldsymbol{\varepsilon}^{\mathrm{p}}} \tag{6.16}$$

with $\mathbf{Q} = \mathrm{diag}[1, 1, 1, 1/2, 1/2, 1/2]$. For most commonly employed flow rules, this definition reduces to

$$\mathrm{d}\kappa = \eta \mathrm{d}\lambda \,, \tag{6.17}$$

with η a positive constant, which depends on the adopted flow rule [23].

Evidently, eq. (6.12), or equivalently (6.15), shows the necessity to compute second-order gradients of the equivalent plastic strain measure κ. One possibility is to use finite differences [5]. The algorithm is then a sequence of separate solutions of the equilibrium problem using finite elements and the plastic yielding problem using finite differences. A more general approach [7,10], is to use only finite elements and to solve the two (coupled) problems simultaneously. For this purpose, it is necessary to employ a weak satisfaction of the yield condition and to discretize the plastic strain field in addition to the standard discretization of the displacement field. Ignoring body forces we obtain:

$$\int_V \delta \mathbf{u}^{\mathrm{T}} (\mathbf{L}^{\mathrm{T}} \boldsymbol{\sigma}_{\mathrm{j+1}}) \, \mathrm{d}V = 0 \tag{6.18}$$

and

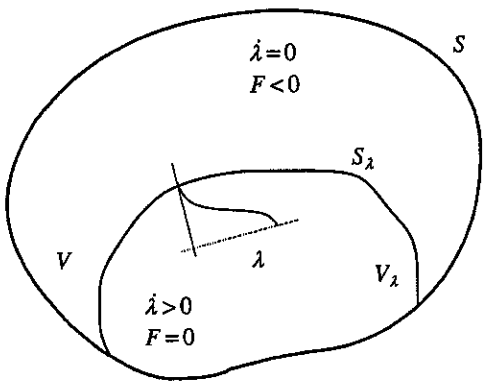

Figure 6.1 Elastic-plastic body with gradient dependence.

$$\int_{V_\lambda} \delta\lambda\, F(\sigma_{j+1}, \kappa_{j+1}, \nabla^2\kappa_{j+1})\, dV = 0\,, \tag{6.19}$$

where the subscript j+1 refers to the current iteration. Unlike in the standard algorithms for plasticity, the yield condition is satisfied in a distributed sense. Furthermore, it is only fulfilled when convergence is reached and not necessarily during the iterative process.

Eq. (6.18) can be modified using integration by parts, the standard boundary conditions $(6.14)_1$, and decomposing σ_{j+1} as $\sigma_j + d\sigma$, where d indicates an increment, i.e. the difference between the values of a variable at the end of iteration j+1 and iteration j:

$$\int_V \delta\boldsymbol{\varepsilon}^T d\sigma\, dV = \int_S \delta\mathbf{u}^T \mathbf{t}_{j+1}\, dS - \int_V \delta\boldsymbol{\varepsilon}^T \sigma_j\, dV\,. \tag{6.20}$$

Using eq. (6.9) we obtain

$$\int_V \delta\boldsymbol{\varepsilon}^T \mathbf{D}^e (d\boldsymbol{\varepsilon} - d\lambda\mathbf{m})\, dV = \int_S \delta\mathbf{u}^T \mathbf{t}_{j+1}\, dS - \int_V \delta\boldsymbol{\varepsilon}^T \sigma_j\, dV\,. \tag{6.21}$$

Now, the yield function F in eq. (6.19) is developed in a Taylor series around $(\sigma_j, \kappa_j, \nabla^2\kappa_j)$ and truncated after the linear terms:

$$F(\sigma_{j+1}, \kappa_{j+1}, \nabla^2\kappa_{j+1}) = F(\sigma_j, \kappa_j, \nabla^2\kappa_j) + \left(\frac{\partial F}{\partial \sigma}\right)^T\Bigg|_j d\sigma$$

$$+ \frac{\partial F}{\partial \kappa}\Bigg|_j d\kappa + \frac{\partial F}{\partial \nabla^2\kappa}\Bigg|_j \nabla^2(d\kappa)\,, \tag{6.22}$$

where $d\kappa = \kappa_{j+1} - \kappa_j$. With the definitions

$$\mathbf{n}=\frac{\partial F}{\partial \boldsymbol{\sigma}}\,, \tag{6.23}$$

$$h=-\frac{\mathrm{d}\kappa}{\mathrm{d}\lambda}\frac{\partial F}{\partial \kappa}=-\eta\frac{\partial F}{\partial \kappa} \tag{6.24}$$

and

$$g=\frac{\mathrm{d}\kappa}{\mathrm{d}\lambda}\frac{\partial F}{\partial \nabla^2\kappa}=\eta\bar{c}\,, \tag{6.25}$$

we obtain the following form of eq. (6.22):

$$F(\sigma_{j+1}\,,\kappa_{j+1}\,,\nabla^2\kappa_{j+1})=F(\sigma_j\,,\kappa_j\,,\nabla^2\kappa_j)+\mathbf{n}^{\mathrm{T}}\mathrm{d}\boldsymbol{\sigma}-h\mathrm{d}\lambda+g\nabla^2(\mathrm{d}\lambda)\,, \tag{6.26}$$

which, after substitution into eq. (6.19), gives the following integral equation:

$$\int_{V_\lambda}\delta\lambda[\mathbf{n}^{\mathrm{T}}\mathbf{D}^{\mathrm{e}}\mathrm{d}\boldsymbol{\varepsilon}-(h+\mathbf{n}^{\mathrm{T}}\mathbf{D}^{\mathrm{e}}\mathbf{m})\mathrm{d}\lambda+g\nabla^2(\mathrm{d}\lambda)]\mathrm{d}V=-\int_{V_\lambda}\delta\lambda F(\sigma_j,\kappa_j,\nabla^2\kappa_j)\mathrm{d}V \tag{6.27}$$

It is noted that the values of $\mathbf{n}$, $\mathbf{m}$, h and g on the left hand side of eq. (6.27) are determined at the end of iteration j, i.e. for the state defined by $(\sigma_j, \kappa_j, \nabla^2\kappa_j)$.

Using integration by parts for the last term on the left hand side of eq. (6.27) we obtain

$$\int_{V_\lambda}\delta\lambda\,[\mathbf{n}^{\mathrm{T}}\mathbf{D}^{\mathrm{e}}\mathrm{d}\boldsymbol{\varepsilon}-(h+\mathbf{n}^{\mathrm{T}}\mathbf{D}^{\mathrm{e}}\mathbf{m})\mathrm{d}\lambda]\,\mathrm{d}V-\int_{V_\lambda}g(\nabla\delta\lambda)^{\mathrm{T}}(\nabla\mathrm{d}\lambda)\,\mathrm{d}V$$

$$=-\int_{V_\lambda}\delta\lambda F(\sigma_j,\kappa_j,\nabla^2\kappa_j)\,\mathrm{d}V \tag{6.28}$$

provided the non-standard boundary conditions

$$\delta\lambda=0 \quad \text{or} \quad (\nabla\mathrm{d}\lambda)^{\mathrm{T}}\boldsymbol{\nu}_\lambda=0 \tag{6.29}$$

are fulfilled on the whole boundary S_λ of the plastic part of the body. The first condition is delicate for finite increments, since the elastic-plastic boundary moves when the plastic zone in the body evolves. During this process the boundary condition $\delta\lambda=0$ on the momentary elastic-plastic boundary may be not true and $(6.29)_2$ must hold. If the same mesh is used for both the equilibrium and yield condition, i.e. if integrals over the whole volume V appear in eqs (6.27) and (6.28), either the admissible $\delta\lambda$ must vanish in the elastic part of the body, which would set constraints on the shape functions to be used, or we must enforce there $F=0$, $\mathbf{n}=\mathbf{0}$ and $\mathrm{d}\lambda=0$.

In the elastic elements $\lambda=0$, so that for spreading of the plastic zone it is important that the numerical solution allows $\nabla^2\lambda>0$ at the elastic-plastic boundary. The dependence of the yield function on the Laplacian of the plastic strain measure is thus essential for the plastification condition and for the determination of the non-standard residual forces on the right hand side of eqs (6.27)/(6.28). The boundary conditions $(6.29)_2$ call for the existence of derivatives of λ as nodal degrees of freedom. Therefore C^1-continuous interpolation functions are necessary for λ whether

eq. (6.27) or eq. (6.28) is discretized. This issue has raised some doubts in the past [10], since the formulation of the variational principle for gradient plasticity [7] suggests that the use of a standard C^0-interpolation for the plastic multiplier is sufficient.

However, it has become clear that it is not enough to symmetrize the tangent stiffness operator to reduce the continuity requirements, but that the residual terms must also be reformulated. For example the yield condition (6.12) in the form

$$F = f(\sigma, \kappa) + g\,\nabla^2 \lambda \tag{6.30}$$

must be recast in an integral form at an element level. To this end F is multiplied by λ and integrated over the element volume. The Laplacian is then eliminated upon integration by parts:

$$\bar{F} = \int_{V_e} \lambda f(\sigma, \kappa)\,\mathrm{d}V - \int_{V_e} g(\nabla\lambda)^{\mathrm{T}}(\nabla\lambda)\,\mathrm{d}V + \int_{S_e} g\lambda(\nabla\lambda)^{\mathrm{T}}\boldsymbol{\nu}_e\,\mathrm{d}S\,. \tag{6.31}$$

Unfortunately, this integral condition cannot perform well in elastic elements, since, numerically, λ is zero there and the second integral gives a negative contribution preventing the yield condition from being violated. It seems that in the standard C^0-approach, without a Laplacian-dependent yield condition, a method of distinguishing the elastic and plastic state is lost, and, consequently, the plastic zone does not spread from the imperfect elements.

If we reformulate the right hand side of eq. (6.28) using the form (6.30) of the yield function as follows

$$-\int_{V_\lambda} \delta\lambda[f(\sigma_{\mathrm{j}}, \kappa_{\mathrm{j}}) + g\nabla^2\lambda_{\mathrm{j}}]\,\mathrm{d}V = -\int_{V_\lambda} \delta\lambda f(\sigma_{\mathrm{j}}, \kappa_{\mathrm{j}})\,\mathrm{d}V$$
$$+\int_{V_\lambda} g(\nabla\delta\lambda)^{\mathrm{T}}(\nabla\lambda_{\mathrm{j}})\mathrm{d}V - \int_{S_\lambda} g\delta\lambda(\nabla\lambda_{\mathrm{j}})^{\mathrm{T}}\boldsymbol{\nu}_\lambda\,\mathrm{d}S\,, \tag{6.32}$$

numerical experiments give incorrect values of the two last terms, since they are equivalent to the Laplacian term which is not well defined if C^1-continuity is not fulfilled.

6.3 C^1-CONTINUOUS ELEMENT FORMULATION

In the field equations (6.21) and (6.27)/(6.28) there appear at most first-order derivatives of the displacements and second-order derivatives of the plastic multiplier. Therefore the discretization procedure for the displacement field $\mathbf{u}$ requires C^0-continuous interpolation functions assembled in $\mathbf{N}$:

$$\mathbf{u} = \mathbf{N}\,\mathbf{a}\,, \tag{6.33}$$

where $\mathbf{a}$ is a nodal displacement vector, and the discretization of the plastic multiplier λ requires C^1-continuous shape functions contained in $\mathbf{h}$

$$\lambda = \mathbf{h}^{\mathrm{T}} \boldsymbol{\Lambda} , \tag{6.34}$$

where $\boldsymbol{\Lambda}$ denotes a vector of nodal degrees of freedom for the plastic multiplier field.

According to the linear kinematic relation (6.8) the discretization of strains has the form:

$$\boldsymbol{\varepsilon} = \mathbf{B}\,\mathbf{a} , \tag{6.35}$$

where $\mathbf{B} = \mathbf{L}\mathbf{N}$. Substitution of the above identities into eq. (6.21) gives the discretized equilibrium condition:

$$\delta \mathbf{a}^{\mathrm{T}} \int_V [\mathbf{B}^{\mathrm{T}} \mathbf{D}^{\mathrm{e}} \mathbf{B} \mathrm{d}\mathbf{a} - \mathbf{B}^{\mathrm{T}} \mathbf{D}^{\mathrm{e}} \mathbf{m} \mathbf{h}^{\mathrm{T}} \mathrm{d}\boldsymbol{\Lambda}]\, \mathrm{d}V = \delta \mathbf{a}^{\mathrm{T}} \int_S \mathbf{N}^{\mathrm{T}} \mathbf{t}_{\mathrm{j+1}}\, \mathrm{d}S - \delta \mathbf{a}^{\mathrm{T}} \int_V \mathbf{B}^{\mathrm{T}} \boldsymbol{\sigma}_{\mathrm{j}}\, \mathrm{d}V . \tag{6.36}$$

Introducing a matrix $\mathbf{q}$ which contains the derivatives of the shape functions in $\mathbf{h}$ we obtain the discretization of the gradient of the plastic multiplier:

$$\nabla \lambda = \mathbf{q}^{\mathrm{T}} \boldsymbol{\Lambda} , \quad \mathbf{q}^{\mathrm{T}} = \nabla \mathbf{h}^{\mathrm{T}} . \tag{6.37}$$

Introducing a vector $\mathbf{p}$ which contains the Laplacians of the shape functions in $\mathbf{h}$ we find the discretization formula for the Laplacian of the plastic multiplier:

$$\nabla^2 \lambda = \mathbf{p}^{\mathrm{T}} \boldsymbol{\Lambda} . \tag{6.38}$$

Substitution of eqs (6.34), (6.35) and (6.38) into eq. (6.27) gives the discretized yield condition in the following form:

$$\delta \boldsymbol{\Lambda}^{\mathrm{T}} \int_V [-\mathbf{h}\mathbf{n}^{\mathrm{T}} \mathbf{D}^{\mathrm{e}} \mathbf{B} \mathrm{d}\mathbf{a} + (h + \mathbf{n}^{\mathrm{T}} \mathbf{D}^{\mathrm{e}} \mathbf{m}) \mathbf{h} \mathbf{h}^{\mathrm{T}} \mathrm{d}\boldsymbol{\Lambda} - g \mathbf{h} \mathbf{p}^{\mathrm{T}} \mathrm{d}\boldsymbol{\Lambda}]\, \mathrm{d}V$$

$$= \delta \boldsymbol{\Lambda}^{\mathrm{T}} \int_V F(\boldsymbol{\sigma}_{\mathrm{j}}, \kappa_{\mathrm{j}}, \nabla^2 \kappa_{\mathrm{j}}) \mathbf{h}\, \mathrm{d}V . \tag{6.39}$$

Eqs (6.36) and (6.39) must hold for any admissible variation of $\delta \mathbf{a}$ and $\delta \boldsymbol{\Lambda}$, so that we obtain the following set of algebraic equations [10]:

$$\begin{bmatrix} \mathbf{K}_{\mathrm{aa}} & \mathbf{K}_{\mathrm{a}\lambda} \\ \mathbf{K}_{\lambda \mathrm{a}} & \mathbf{K}_{\lambda\lambda} \end{bmatrix} \begin{bmatrix} \mathrm{d}\mathbf{a} \\ \mathrm{d}\boldsymbol{\Lambda} \end{bmatrix} = \begin{bmatrix} \mathbf{f}_{\mathrm{e}} + \mathbf{f}_{\mathrm{a}} \\ \mathbf{f}_{\lambda} \end{bmatrix} , \tag{6.40}$$

with the elastic stiffness matrix:

$$\mathbf{K}_{\mathrm{aa}} = \int_V \mathbf{B}^{\mathrm{T}} \mathbf{D}^{\mathrm{e}} \mathbf{B}\, \mathrm{d}V , \tag{6.41}$$

the off-diagonal matrices:

$$\mathbf{K}_{\mathrm{a}\lambda} = -\int_V \mathbf{B}^{\mathrm{T}} \mathbf{D}^{\mathrm{e}} \mathbf{m} \mathbf{h}^{\mathrm{T}}\, \mathrm{d}V , \quad \mathbf{K}_{\lambda \mathrm{a}} = -\int_V \mathbf{h}\mathbf{n}^{\mathrm{T}} \mathbf{D}^{\mathrm{e}} \mathbf{B}\, \mathrm{d}V , \tag{6.42}$$

the nonsymmetric gradient-dependent matrix:

$$\mathbf{K}_{\lambda\lambda} = \int_V [(h + \mathbf{n}^T \mathbf{D}^e \mathbf{m})\mathbf{h}\mathbf{h}^T - g\mathbf{h}\mathbf{p}^T]\, dV \ , \tag{6.43}$$

the external force vector and the vector of nodal forces equivalent to internal stresses:

$$\mathbf{f}_e = \int_S \mathbf{N}^T \mathbf{t}_{j+1}\, dS \ , \quad \mathbf{f}_a = -\int_V \mathbf{B}^T \boldsymbol{\sigma}_j\, dV \ , \tag{6.44}$$

and the vector of residual forces emerging from the inexact fulfilment of the yield condition:

$$\mathbf{f}_\lambda = \int_V F(\boldsymbol{\sigma}_j, \kappa_j, \nabla^2 \kappa_j)\, \mathbf{h}\, dV \ . \tag{6.45}$$

If we make use of eq. (6.28) instead of eq. (6.27), substitution of eqs (6.34), (6.35) and (6.37) gives the second form of the discretized yield condition:

$$\delta\boldsymbol{\Lambda}^T \int_V [-\mathbf{h}\mathbf{n}^T \mathbf{D}^e \mathbf{B} d\mathbf{a} + (h + \mathbf{n}^T \mathbf{D}^e \mathbf{m})\mathbf{h}\mathbf{h}^T d\boldsymbol{\Lambda} + g\mathbf{q}\mathbf{q}^T d\boldsymbol{\Lambda}]\, dV$$

$$= \delta\boldsymbol{\Lambda}^T \int_V F(\boldsymbol{\sigma}_j, \kappa_j, \nabla^2 \kappa_j)\mathbf{h}\, dV, \tag{6.46}$$

which leads to a similar matrix problem as in eq. (6.40), but now the nonsymmetry due to the Laplacian term vanishes, i.e. the matrix $\mathbf{K}_{\lambda\lambda}$ is nonsymmetric only for non-associated flow:

$$\mathbf{K}_{\lambda\lambda} = \int_V [(h + \mathbf{n}^T \mathbf{D}^e \mathbf{m})\mathbf{h}\mathbf{h}^T + g\mathbf{q}\mathbf{q}^T]\, dV \ . \tag{6.47}$$

However, the additional boundary conditions (6.29) have to be enforced in this case.

The set of equations (6.40) governs the element behaviour during the plastic flow. We will now consider the actual problem of a structure which is initially elastic and then, due to an inhomogeneous stress distribution, exhibits a partial plastification. If all elements are elastic, we have $\mathbf{K}_{\lambda a} = \mathbf{0}$ and $\mathbf{K}_{a\lambda} = \mathbf{0}$ since the gradient vectors $\mathbf{m}$ and $\mathbf{n}$ are set to zero. We obtain from eq. (6.40) the classical set of equations in $d\mathbf{a}$

$$\mathbf{K}_{aa}\, d\mathbf{a} = \mathbf{f}_e + \mathbf{f}_a \tag{6.48}$$

and the additional set of equations in $d\boldsymbol{\Lambda}$

$$\mathbf{K}^e_{\lambda\lambda}\, d\boldsymbol{\Lambda} = \mathbf{f}_\lambda \ . \tag{6.49}$$

For the elastic state we have $F < 0$ and the residual forces $\mathbf{f}_\lambda$ are set equal to zero. Eq. (6.49) then yields the desired solution $d\boldsymbol{\Lambda} = \mathbf{0}$ if the global matrix $\hat{\mathbf{K}}^e$ is nonsingular after the element assembly and after the introduction of boundary conditions for the $\boldsymbol{\Lambda}$ degrees of freedom. The explicit introduction of boundary conditions is always necessary for the symmetric formulation, and may be necessary for the nonsymmetric formulation.

When plastic elements appear in the structure, then in elastic elements adjacent to the plastic zone we have $\mathbf{f}_\lambda \neq \mathbf{0}$ and we obtain non-zero $\mathrm{d}\boldsymbol{\Lambda}$ from eq. (6.49). The C^1-continuous finite elements have the feature, that these nodal values of plastic multiplier $\mathrm{d}\boldsymbol{\Lambda}$ yield $\mathrm{d}\lambda \approx 0$ and $\nabla^2(\mathrm{d}\lambda)>0$ at the integration points. As a result the gradient-dependent yield strength $\bar{\sigma}_g = \bar{\sigma} - g\nabla^2\lambda$ is reduced and new elastic elements can enter the plastic regime.

It is noted that it is not necessary to set the value of hardening modulus h equal to a large number in the formula (6.43) to constrain the value of λ to zero for elastic elements (cf. [10]). In fact, this substitution adversely affects the conditioning of the global tangential operator, which affects the accuracy of the stress point algorithm to be discussed in a subsequent section. For some elements it may cause containment of the plastic flow in the initially imperfect zones and prevent the regularization effect. Based on recent experience, it is suggested to set h equal to Young's modulus E for elastic elements. The gradient term may be neglected in the matrix $\mathbf{K}^e_{\lambda\lambda}$ for elastic elements, since its inclusion only slightly influences the results. Using numerical integration the matrix $\mathbf{K}^e_{\lambda\lambda}$ is then determined as:

$$\mathbf{K}^e_{\lambda\lambda} = \sum_{ip=1}^{np} E\, \mathbf{h}_{ip}\mathbf{h}_{ip}^{\mathrm{T}}\, V_{ip}\,, \tag{6.50}$$

where V_{ip} is the volume contribution of an integration point.

It is useful to examine the rank of submatrices $\mathbf{K}_{aa}$ and $\mathbf{K}^e_{\lambda\lambda}$ in order to determine the number of integration points and extra boundary conditions sufficient to avoid spurious modes for both the displacement and plastic multiplier fields. The elastic stiffness matrix $\mathbf{K}_{aa}$ should have zero eigenvalues associated only with the rigid body modes. The matrix $\mathbf{K}^e_{\lambda\lambda}$ should have a number of non-zero eigenvalues which is equal to the number of integration points (matrix $\mathbf{h}\mathbf{h}^{\mathrm{T}}$ has only one non-zero eigenvalue). As we will see in the following, some elements do not satisfy these requirements.

It should also be taken into account, that a high-order integration scheme and too many additional boundary conditions for λ, even if they comply with the theory, can lead to an overconstrained plastic flow problem and have a negative influence on the accuracy of finite element predictions. Since the yield condition can be conceived as a differential constraint to the equilibrium condition of a nonlinear solid, the number of constraints for the plastic multiplier field must be limited, otherwise the solution will be inaccurate or will lock, just as can happen for some standard elements under the isochoric deformations. In other words, we now have a two-field theory similar to the mixed formulation with independent displacement and pressure interpolations. A proper constraint ratio between the λ degrees of freedom and the displacement degrees of freedom must therefore be maintained.

6.4 C^0-CONTINUOUS ELEMENT FORMULATION

In order to be able to use C^0-continuous interpolation functions for the plastic multiplier field, we introduce new variables φ_x, φ_y and φ_z:

$$\varphi_x = \frac{\partial \lambda}{\partial x}, \quad \varphi_y = \frac{\partial \lambda}{\partial y}, \quad \varphi_z = \frac{\partial \lambda}{\partial z} \tag{6.51}$$

and collect them in a vector $\boldsymbol{\phi} = (\varphi_x, \varphi_y, \varphi_z)$. In this way we can write the gradient of the plastic multiplier as

$$\nabla \lambda = \boldsymbol{\phi} \tag{6.52}$$

and represent the Laplacian of λ as

$$\nabla^2 \lambda = \frac{\partial \varphi_x}{\partial x} + \frac{\partial \varphi_y}{\partial y} + \frac{\partial \varphi_z}{\partial z} = \nabla^{\mathrm{T}} \boldsymbol{\phi}, \tag{6.53}$$

where the scalar product of the operator ∇^{T} and the vector field $\boldsymbol{\phi}$ denotes the divergence operator. The result of eq. (6.53) can be substituted in eq. (6.27) or (6.28), but the constraint (6.52) must be added to the formulation.

Since the first version of our problem is nonsymmetric and since we want to avoid the introduction of a Lagrangian multiplier field in addition to the already defined three fields $\mathbf{u}$, λ and $\boldsymbol{\phi}$, we will make use of the penalty approach. We can include the constraint by means of an additional variational equation:

$$\int_V k(\nabla \lambda - \boldsymbol{\phi})^{\mathrm{T}} [\nabla(\delta \lambda) - \delta \boldsymbol{\phi}] \, \mathrm{d}V = 0, \tag{6.54}$$

where k is a penalty factor. In computations we use $k = E^3$, where E is Young's modulus. Using the incremental form of eq. (6.54) together with eqs (6.21) and (6.27) we obtain a set of three integral equations:

$$\int_V \delta \boldsymbol{\varepsilon}^{\mathrm{T}} \mathbf{D}^{\mathrm{e}} (\mathrm{d}\boldsymbol{\varepsilon} - \mathrm{d}\lambda \mathbf{m}) \, \mathrm{d}V = \int_S \delta \mathbf{u}^{\mathrm{T}} \mathbf{t}_{\mathrm{j+1}} \, \mathrm{d}S - \int_V \delta \boldsymbol{\varepsilon}^{\mathrm{T}} \boldsymbol{\sigma}_{\mathrm{j}} \, \mathrm{d}V, \tag{6.55}$$

$$\int_V \delta \lambda \, [\mathbf{n}^{\mathrm{T}} \mathbf{D}^{\mathrm{e}} \mathrm{d}\boldsymbol{\varepsilon} - (h + \mathbf{n}^{\mathrm{T}} \mathbf{D}^{\mathrm{e}} \mathbf{m}) \mathrm{d}\lambda + g \nabla^{\mathrm{T}} \, \mathrm{d}\boldsymbol{\phi}] \mathrm{d}V = - \int_V \delta \lambda F(\boldsymbol{\sigma}_{\mathrm{j}}, \kappa_{\mathrm{j}}, \nabla^2 \kappa_{\mathrm{j}}) \mathrm{d}V \tag{6.56}$$

where according to eqs (6.17) and (6.53) we calculate $\nabla^2 \kappa = \eta \nabla^{\mathrm{T}} \boldsymbol{\phi}$ and

$$k \int_V \delta \lambda \, \nabla^{\mathrm{T}} [\nabla(\mathrm{d}\lambda) - \mathrm{d}\boldsymbol{\phi}] \, \mathrm{d}V - k \int_V \delta \boldsymbol{\phi}^{\mathrm{T}} [\nabla(\mathrm{d}\lambda) - \mathrm{d}\boldsymbol{\phi}] \, \mathrm{d}V = 0. \tag{6.57}$$

The above equations are discretized using the formulas (6.34), (6.35) and (6.37), but now with C^0-continuous shape functions in $\mathbf{h}$, and the following interpolation for the new variables in $\boldsymbol{\phi}$:

$$\boldsymbol{\phi} = \mathbf{P} \boldsymbol{\Phi}, \tag{6.58}$$

where $\boldsymbol{\Phi}$ contains the nodal values of φ_x, φ_y and φ_z and $\mathbf{P}$ is a matrix of shape functions, similar to $\mathbf{N}$. Upon the discretization of eqs (6.55)-(6.57) and the usual argument that the resulting equations

$$\delta\mathbf{a}^{\mathrm{T}}\int_V[\mathbf{B}^{\mathrm{T}}\mathbf{D}^{\mathrm{e}}\mathbf{B}\mathrm{d}\mathbf{a}-\mathbf{B}^{\mathrm{T}}\mathbf{D}^{\mathrm{e}}\mathbf{m}\mathbf{h}^{\mathrm{T}}\mathrm{d}\Lambda]\,\mathrm{d}V=\delta\mathbf{a}^{\mathrm{T}}\int_S\mathbf{N}^{\mathrm{T}}\mathbf{t}_{j+1}\,\mathrm{d}V-\delta\mathbf{a}^{\mathrm{T}}\int_V\mathbf{B}^{\mathrm{T}}\boldsymbol{\sigma}_j\,\mathrm{d}V \tag{6.59}$$

$$\delta\Lambda^{\mathrm{T}}\int_V[-\mathbf{h}\mathbf{n}^{\mathrm{T}}\mathbf{D}^{\mathrm{e}}\mathbf{B}\mathrm{d}\mathbf{a}+(h+\mathbf{n}^{\mathrm{T}}\mathbf{D}^{\mathrm{e}}\mathbf{m})\mathbf{h}\mathbf{h}^{\mathrm{T}}\mathrm{d}\Lambda-g\mathbf{h}\nabla^{\mathrm{T}}\mathbf{P}\,\mathrm{d}\Phi]\,\mathrm{d}V=$$

$$=\delta\Lambda^{\mathrm{T}}\int_V F(\boldsymbol{\sigma}_j,\kappa_j,\nabla^2\kappa_j)\mathbf{h}\,\mathrm{d}V \tag{6.60}$$

and

$$k\,\delta\Lambda^{\mathrm{T}}\int_V\mathbf{q}(\mathbf{q}^{\mathrm{T}}\mathrm{d}\Lambda-\mathbf{P}\,\mathrm{d}\Phi)\,\mathrm{d}V-k\,\delta\Phi^{\mathrm{T}}\int_V\mathbf{P}^{\mathrm{T}}(\mathbf{q}^{\mathrm{T}}\mathrm{d}\Lambda-\mathbf{P}\,\mathrm{d}\Phi)\,\mathrm{d}V=0 \tag{6.61}$$

must hold for any admissible $\delta\mathbf{a}$, $\delta\Lambda$ and $\delta\Phi$, we obtain the following set of algebraic equations in a matrix form:

$$\left\{\begin{bmatrix}\mathbf{K}_{aa} & \mathbf{K}_{a\lambda} & \mathbf{0}\\ \mathbf{K}_{\lambda a} & \mathbf{K}_{\lambda\lambda} & \mathbf{K}_{\lambda\varphi}\\ \mathbf{0} & \mathbf{0} & \mathbf{0}\end{bmatrix}+k\begin{bmatrix}\mathbf{0} & \mathbf{0} & \mathbf{0}\\ \mathbf{0} & \mathbf{K}^{\mathrm{c}}_{\lambda\lambda} & \mathbf{K}^{\mathrm{c}}_{\lambda\varphi}\\ \mathbf{0} & \mathbf{K}^{\mathrm{cT}}_{\lambda\varphi} & \mathbf{K}^{\mathrm{c}}_{\varphi\varphi}\end{bmatrix}\right\}\begin{bmatrix}\mathrm{d}\mathbf{a}\\ \mathrm{d}\Lambda\\ \mathrm{d}\Phi\end{bmatrix}=\begin{bmatrix}\mathbf{f}_e+\mathbf{f}_a\\ \mathbf{f}_\lambda\\ \mathbf{0}\end{bmatrix}. \tag{6.62}$$

In eq. (6.62) the submatrices $\mathbf{K}_{aa}$, $\mathbf{K}_{a\lambda}$ and $\mathbf{K}_{\lambda a}$ are given in eqs (6.41) and (6.42). $\mathbf{K}_{\lambda\lambda}$ and $\mathbf{K}_{\lambda\varphi}$ are defined as

$$\mathbf{K}_{\lambda\lambda}=\int_V(h+\mathbf{n}^{\mathrm{T}}\mathbf{D}^{\mathrm{e}}\mathbf{m})\mathbf{h}\mathbf{h}^{\mathrm{T}}\,\mathrm{d}V\,,\quad \mathbf{K}_{\lambda\varphi}=-\int_V[g\mathbf{h}\nabla^{\mathrm{T}}\mathbf{P}]\,\mathrm{d}V\,, \tag{6.63}$$

and the submatrices with the superscript c in the additional (symmetric) matrix introducing the constraint (6.52) are defined as

$$\mathbf{K}^{\mathrm{c}}_{\lambda\lambda}=\int_V\mathbf{q}\,\mathbf{q}^{\mathrm{T}}\,\mathrm{d}V\,,\quad \mathbf{K}^{\mathrm{c}}_{\varphi\varphi}=\int_V\mathbf{P}^{\mathrm{T}}\mathbf{P}\,\mathrm{d}V\,,\quad \mathbf{K}^{\mathrm{c}}_{\lambda\varphi}=\int_V-\mathbf{q}\,\mathbf{P}\,\mathrm{d}V\,. \tag{6.64}$$

In this formulation all the interpolation functions in $\mathbf{N}$, $\mathbf{h}$ and $\mathbf{P}$ are C^0-continuous.

If we substitute the new variables from eq. (6.52) into eq. (6.28), which is the starting point for the symmetric formulation, we obtain the weak form of the yield condition:

$$\int_V\delta\lambda[\mathbf{n}^{\mathrm{T}}\mathbf{D}^{\mathrm{e}}\mathrm{d}\varepsilon-(h+\mathbf{n}^{\mathrm{T}}\mathbf{D}^{\mathrm{e}}\mathbf{m})\mathrm{d}\lambda]\mathrm{d}V-\int_V g\delta\phi\mathrm{d}\phi\mathrm{d}V \tag{6.65}$$

$$=-\int_V\delta\lambda F(\boldsymbol{\sigma}_j,\kappa_j,\nabla^2\kappa_j)\mathrm{d}V, \tag{6.66}$$

in which the derivatives of ϕ appear only on the right hand side. Substitution of the discretization formulas (6.34), (6.35) and (6.58) gives the symmetric form of the discretized yield condition:

$$\delta\Lambda^{\mathrm{T}} \int_V [-\mathbf{h}\mathbf{n}^{\mathrm{T}}\mathbf{D}^{\mathrm{e}}\mathbf{B}\mathrm{d}\mathbf{a} + (h + \mathbf{n}^{\mathrm{T}}\mathbf{D}^{\mathrm{e}}\mathbf{m})\mathbf{h}\mathbf{h}^{\mathrm{T}}\mathrm{d}\Lambda]\,\mathrm{d}V + \int_V g\delta\Phi^{\mathrm{T}}\mathbf{P}^{\mathrm{T}}\mathbf{P}\,\mathrm{d}\Phi\,\mathrm{d}V =$$

$$= \delta\Lambda^{\mathrm{T}} \int_V F(\sigma_{\mathrm{j}}, \kappa_{\mathrm{j}}, \nabla^2\kappa_{\mathrm{j}})\,\mathbf{h}\,\mathrm{d}V\ . \tag{6.67}$$

The (symmetric) tangent operator now reads:

$$\left\{ \begin{bmatrix} \mathbf{K}_{\mathrm{aa}} & \mathbf{K}_{\mathrm{a}\lambda} & \mathbf{0} \\ \mathbf{K}_{\lambda\mathrm{a}} & \mathbf{K}_{\lambda\lambda} & \mathbf{0} \\ \mathbf{0} & \mathbf{0} & \mathbf{K}_{\varphi\varphi} \end{bmatrix} + k \begin{bmatrix} \mathbf{0} & \mathbf{0} & \mathbf{0} \\ \mathbf{0} & \mathbf{K}^{\mathrm{c}}_{\lambda\lambda} & \mathbf{K}^{\mathrm{c}}_{\lambda\varphi} \\ \mathbf{0} & \mathbf{K}^{\mathrm{cT}}_{\lambda\varphi} & \mathbf{K}^{\mathrm{c}}_{\varphi\varphi} \end{bmatrix} \right\} \begin{bmatrix} \mathrm{d}\mathbf{a} \\ \mathrm{d}\Lambda \\ \mathrm{d}\Phi \end{bmatrix} = \begin{bmatrix} \mathbf{f}_{\mathrm{e}} + \mathbf{f}_{\mathrm{a}} \\ \mathbf{f}_{\lambda} \\ \mathbf{0} \end{bmatrix}, \tag{6.68}$$

where

$$\mathbf{K}_{\varphi\varphi} = \int_V g\mathbf{P}^{\mathrm{T}}\mathbf{P}\,\mathrm{d}V \tag{6.69}$$

and all the other submatrices have been defined previously. With the set (6.68) the additional boundary conditions (6.29), now written as:

$$\delta\mathrm{d}\lambda = 0 \quad \text{or} \quad \mathrm{d}\boldsymbol{\phi}^{\mathrm{T}}\boldsymbol{\nu}_{\lambda} = 0 \tag{6.70}$$

must be fulfilled on the boundary S_{λ} of the plastic part of the body.

It is important that for the penalty method to be successful the penalty submatrix $\mathbf{K}^{\mathrm{c}}$ must be singular. Otherwise non-zero $\boldsymbol{\Phi}$ values are not admitted. To achieve this goal reduced numerical integration should be used (cf. [11]). Since the penalty constraint assures the satisfaction of eq. (6.52) only in the sampling points, the best results are expected when uniformly reduced integration is employed for all the matrices.

As explained in the previous section, the sets of equations (6.62) and (6.68) are also required to hold in the elastic subdomain. We should have a sufficient rank of the elastic stiffness matrix $\mathbf{K}_{\mathrm{aa}}$ to prevent the presence of spurious deformation modes. Simultaneously we should have a sufficient rank of the matrix $\mathbf{K}^{\mathrm{e}}_{\lambda\lambda}$ from eq. (6.50) to prevent the presence of the spurious non-zero modes of both λ and $\boldsymbol{\phi}$ in the elastic elements. This suggests the use of a full integration scheme, but in view of the argument that the penalty submatrix $\mathbf{K}^{\mathrm{c}}$ must be singular, we must then resort to extra boundary conditions. It also turns out advantageous to include the gradient submatrix $\mathbf{K}_{\lambda\varphi}$ (or $\mathbf{K}_{\varphi\varphi}$) in the tangent operator for the elastic elements, since it perturbs the singularity of the tangent operator in eqs (6.62) and (6.68), making the emergence of the spurious modes more difficult.

It is noted that for a two-dimensional case the element structure in this approach shows similarities with the Reissner-Mindlin plate bending elements [12] and that the penalty method has been also used within the context of plate bending to introduce the Kirchhoff constraints in the formulation [13].

6.5 STRESS-STRAIN RELATION AND TANGENT OPERATOR

As in standard elasto-plasticity the stress update is computed as an integral along a given path from the initial state defined by $(\boldsymbol{\varepsilon}_0, \boldsymbol{\sigma}_0)$ to the final state:

$$\boldsymbol{\sigma} = \boldsymbol{\sigma}_0 + \int_{\boldsymbol{\varepsilon}_0}^{\boldsymbol{\varepsilon}} \mathbf{D}^{ep}\, d\boldsymbol{\varepsilon} \,, \tag{6.71}$$

where the continuous tangent operator is defined as

$$\mathbf{D}^{ep} = \left.\frac{\partial \boldsymbol{\sigma}}{\partial \boldsymbol{\varepsilon}}\right|_{\boldsymbol{\varepsilon}} \,. \tag{6.72}$$

Algorithmically, the stress is updated according to:

$$\boldsymbol{\sigma}_j = \boldsymbol{\sigma}_0 + \mathbf{S}(\boldsymbol{\varepsilon}_0, \Delta\boldsymbol{\varepsilon}_j) \,, \tag{6.73}$$

where $\mathbf{S}$ is a nonlinear mapping operator, which depends on the numerical method of plastic strain integration within the increment (e.g. generalized midpoint rule), and Δ denotes a 'total' increment, which is a sum of 'delta' increments in the iterations:

$$\Delta\boldsymbol{\varepsilon}_j = \sum_{i=1}^{j} d\boldsymbol{\varepsilon}_i \,. \tag{6.74}$$

The consistent (algorithmic) tangent operator is then defined as [14,15]:

$$\mathbf{D}^{cons}(\boldsymbol{\varepsilon}_0, \Delta\boldsymbol{\varepsilon}_j) = \left.\frac{\partial \boldsymbol{\sigma}_j}{\partial \Delta\boldsymbol{\varepsilon}}\right|_{\boldsymbol{\varepsilon}_0, \Delta\boldsymbol{\varepsilon}_j} = \left.\frac{\partial \mathbf{S}}{\partial \Delta\boldsymbol{\varepsilon}}\right|_{\boldsymbol{\varepsilon}_0, \Delta\boldsymbol{\varepsilon}_j} \tag{6.75}$$

and is in general nonsymmetric. For finite, especially large, steps the operator $\mathbf{D}^{cons}$ differs significantly from the continuous operator $\mathbf{D}^{ep}$. To achieve a quadratic convergence rate of Newton's algorithm used for the solution of the set of incremental equations the consistent linearization as above must be performed.

The Euler backward algorithm

$$\boldsymbol{\sigma}_j = \boldsymbol{\sigma}_0 + \mathbf{D}^e \Delta\boldsymbol{\varepsilon}_j - \Delta\lambda_j \mathbf{D}^e \mathbf{m}_j \,, \tag{6.76}$$

used in the gradient plasticity algorithm to calculate $\boldsymbol{\sigma}_j$ at an integration point, falls within the format (6.73). Therefore, the algorithmic tangent operator can be derived according to (6.75) and reads:

$$\mathbf{D}^{cons} = \mathbf{H} - \frac{\mathbf{H}\mathbf{m}\mathbf{n}^T\mathbf{H}}{h + \mathbf{n}^T\mathbf{H}\mathbf{m}} \,, \tag{6.77}$$

with $\mathbf{H}$ a pseudo-elastic stiffness operator:

$$\mathbf{H} = \left[(\mathbf{D}^e)^{-1} + \Delta\lambda \frac{\partial \mathbf{m}}{\partial \boldsymbol{\sigma}} \right]^{-1} \,, \tag{6.78}$$

Box 6.1. An algorithm for gradient plasticity.

1. Compute $\mathbf{K}_{aa}$, $\mathbf{K}_{a\lambda}$, $\mathbf{K}_{\lambda a}$, $\mathbf{K}_{\lambda\lambda}$, $\mathbf{f}_e$, $\mathbf{f}_a$ $\mathbf{f}_\lambda$.

2. Solve for da and $d\Lambda$ and update $\Delta\mathbf{a}_j = \Delta\mathbf{a}_{j-1} + d\mathbf{a}$, $\Delta\Lambda_j = \Delta\Lambda_{j-1} + d\Lambda$.

3. For each integration point compute:

$$\Delta\boldsymbol{\varepsilon}_j = \mathbf{B}\Delta\mathbf{a}_j,$$

$$\Delta\lambda_j = \mathbf{h}^T\Delta\boldsymbol{\Lambda}_j,$$

$$\nabla^2(\Delta\lambda_j) = \mathbf{p}^T\Delta\boldsymbol{\Lambda}_j,$$

$$\kappa_j = \kappa_0 + \eta\Delta\lambda_j,$$

$$\nabla^2\kappa_j = \nabla^2\kappa_0 + \eta\nabla^2(\Delta\lambda_j),$$

$$\boldsymbol{\sigma}_t = \boldsymbol{\sigma}_0 + \mathbf{D}^e\Delta\boldsymbol{\varepsilon}_j \text{ (trial stress).}$$

If $F(\boldsymbol{\sigma}_t, \kappa_j, \nabla^2\kappa_j) \geq -\varepsilon$,

then plastic state: $\boldsymbol{\sigma}_j = \boldsymbol{\sigma}_t - \Delta\lambda_j\mathbf{D}^e\mathbf{m}_t$,

else elastic state: $\boldsymbol{\sigma}_j = \boldsymbol{\sigma}_t$.

4. Check global convergence criterion. If not converged, go to 1.

where the subscript j has been skipped for convenience. In the present gradient plasticity algorithm the elastic stiffness matrix $\mathbf{D}^e$ is thus replaced by the algorithmic operator $\mathbf{H}$ in the equilibrium equation (6.21) and in the consistency condition (6.27)/(6.28).

The solution procedure that ensues from this algorithm is presented in Box 6.1 for C^1-continuous gradient plasticity elements The algorithm for C^0-elements is similar. For integration points in an elastic state an artificial hardening modulus $h = E$ is substituted in submatrix $\mathbf{K}_{\lambda\lambda}$ of the tangent operator to avoid singularity. The flow direction $\mathbf{m}$ is approximated by $\mathbf{m}_t = \mathbf{m}(\boldsymbol{\sigma}_t)$, its value in the trial stress state $\boldsymbol{\sigma}_t = \boldsymbol{\sigma}_0 + \mathbf{D}^e\Delta\boldsymbol{\varepsilon}_j$.

The update of the nodal variables is done in a 'total-incremental' way, i.e. in every iteration total increments from the equilibrium state at the end of the previous loading step are calculated. The values of κ_j and $\nabla^2\kappa_j$ are also updated using 'total' increments. The advantage of this approach is that spurious unloading is avoided. The increment of plastic multiplier $\Delta\lambda$ is directly determined from the nodal values of $\Delta\boldsymbol{\Lambda}$. The stresses are computed starting from the equilibrium state $\boldsymbol{\sigma}_0$. For integration points in a plastic state the idea of elastic predictor (trial stress $\boldsymbol{\sigma}_t$) and plastic corrector (return mapping) $-\Delta\lambda\mathbf{D}^e\mathbf{m}$ is followed. The updated values of the hardening parameter κ_j and its Laplacian $\nabla^2\kappa_j$ are already available at the trial stress state and are used in the yield condition. Alternatively, the memorized values from the previous increment κ_0 and $\nabla^2\kappa_0$ can be used, which results in a slightly delayed plastification. The relation of the present algorithm to the tangent-

cutting-plane algorithm [16] is not so close as in the 'delta-incremental' algorithm used by de Borst and Mühlhaus [10].

Because the plastic multiplier is an independent variable determined in the solution of the global set of equations, the weak form of the yield condition (6.19) is not satisfied until convergence is achieved. It can happen that, due to stress redistribution or nonlinear softening, the increment $\Delta\lambda$ results in a return mapping to the inside of the yield surface. In the present total-incremental algorithm this does not cause the detection of unloading, but changes sign of the residual forces, which results further in a proper correction (decrease) of $\Delta\lambda$. However, difficulties may arise, if the value of the yield function has different signs at the integration points within one element. The respective contributions to residual force $\mathbf{f}_\lambda$ are then averaged because of the weak formulation and improper values of corrections $\mathrm{d}\boldsymbol{\Lambda}$ are obtained from the global set of equations. Therefore, the best convergence is found for those finite elements in which, at the sampling points, the value of the yield function F converges to zero with the decrease of the residual force norm.

6.6 SOME ELEMENTS FOR GRADIENT PLASTICITY

6.6.1 One-dimensional elements

Figure 6.2 shows the simplest one-dimensional gradient plasticity elements with C^1-continuity. The axial displacement u is interpolated linearly or quadratically and for the plastic multiplier λ the cubic hermitian shape functions are used.

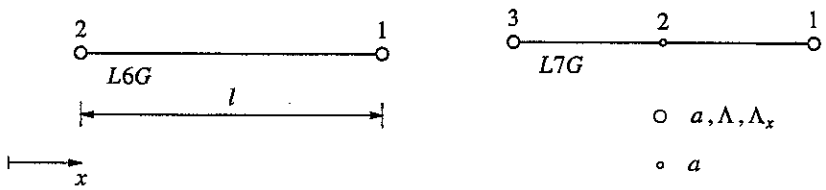

Figure 6.2 One-dimensional C^1-elements.

For element $L6G$ two-point Gaussian integration is employed. Matrix $\mathbf{K}_{\lambda\lambda}$ includes polynomials of the 6^{th}-order and is not integrated accurately. Translation in the x-direction must be prevented and two additional constraints (e.g. symmetry) or boundary conditions for the λ field must be introduced in a model. The number of extra constraints is determined as follows: 2×2 degrees of freedom for λ minus 2×1 relations in Gauss points equals 2. The element yields an exact fulfilment of the yield condition at the integration points, which means that when $\mathbf{f}_\lambda \to 0$, then $F_{\mathrm{ip}} \to 0$, but stress oscillations are observed. This phenomenon may cause a failure of convergence at an early stage of softening as soon as the oscillating stresses reach a state with $\bar{\sigma}_{\mathrm{g}} \to 0$.

For element $L7G$ with two-point integration the balance between the interpolation for u and λ is optimal, i.e. the stress integration in eq. (6.76) gives a stress state σ_{j}, which is constant within an element and which fulfils exactly the yield condition. Convergence in one iteration is observed unless the softening zone spreads or

nonlinear softening is used. This behaviour is attributed to the special qualities of the integration stations, so-called Barlow points [17], in which higher order accuracy of interpolated field derivatives is obtained. In fact, these are the only points, in which the third-order terms in $F(\sigma_j, \kappa_j, \nabla^2\kappa_j)$ cancel the first-order terms, so that the yield function equals zero.

The above properties are exhibited by the nonsymmetric formulation with $\mathbf{K}_{\lambda\lambda}$ from eq. (6.43). If the symmetric format for $\mathbf{K}_{\lambda\lambda}$ according to eq. (6.47) is used together with the required boundary conditions and two-point (reduced) integration, convergence is lost. This behaviour is attributed to an unfavourable numerical integration error, since for three-point integration the symmetric and nonsymmetric formulation give the same results. However, for the three-point integration too many constraints are introduced and the results are inaccurate. The stresses at one or more points are then mapped to the inside of the yield surface ($F_j < 0$), which violates the Kuhn-Tucker conditions (6.13) and results in a disturbance of convergence.

Figure 6.3 shows the one-dimensional C^0-elements with separate Lagrange interpolation of the longitudinal displacement u, the plastic multiplier λ and the additional variable φ. Element $L6C$ uses linear shape functions and one integration point. It is the point, in which the constraint $\varphi = \lambda_{,x}$ is fulfilled. The longitudinal translation must be prevented and two boundary conditions for λ or φ should be introduced in a model: 2×3 degrees of freedom minus 3 relations in the Gauss point equals 3; the tangent operator for an elastic element has 3 zero eigenvalues. The element is perfectly convergent since the integration station is a Barlow point [17]. Element $L9C$ uses quadratic shape functions and two Gauss points, which are again optimal for convergence. Boundary conditions similar to the $L6C$ element must be introduced and the return mapping is also exact. In presence of the additional boundary conditions (6.70) the symmetric and nonsymmetric formulations give the same results for the one-dimensional C^0-elements, because the employed numerical integration schemes are sufficient for an exact integration of the shape function polynomials.

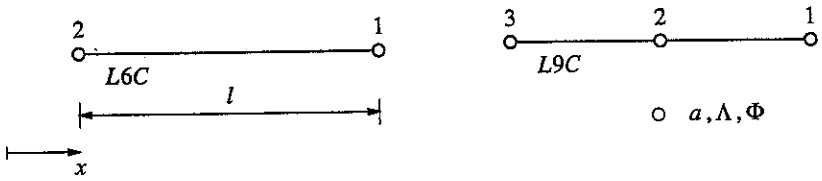

Figure 6.3 One-dimensional C^0-elements with constraint.

6.6.2 Quadrilateral elements

Figure 6.4 shows a family of rectangular elements with a varying interpolation of the displacements and the same bi-hermitian shape functions for the plastic strain field. The elements are formulated in a Cartesian global reference system and cannot be transformed because of the presence of the mixed derivative degrees of

freedom Λ_{xy} in the C^1-interpolation of λ. Only the nonsymmetric formulation of the problem yields fully convergent results.

Element *R*24_*G* [18] employs bilinear interpolation of displacements and 2×2 point integration (notice that the names of the plane stress and plane strain versions of the elements are obtained by substitution of *M* and *E*, respectively, for the underscore mark). To avoid volumetric locking in plane strain problems, $\bar{B}$-enhancement is used [11]. To avoid shear locking, the shear terms are integrated using only one Gauss point. Matrix $\mathbf{K}_{aa}$ possesses the correct rank, see also the discussion after eq. (6.50). The matrix $\mathbf{K}^e_{\lambda\lambda}$ requires 12 additional constraints (4×4 - 4×1 = 12) and they can be introduced by extra boundary conditions for derivatives of λ. For an arbitrary assembly the conditions $\Lambda_n = 0$ and $\Lambda_{xy} = 0$ on the whole model boundary supply exactly the required number of constraints. Element *R*24_*G* gives $F_{ip} \to 0$, but as the one-dimensional element *L*6*G* it shows stress oscillations due to the lack of balance between the employed interpolations.

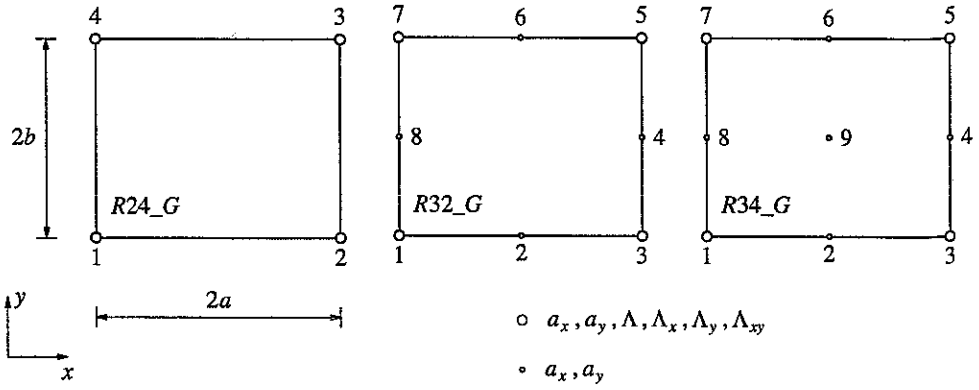

Figure 6.4 Rectangular C^1-elements.

Element *R*32_*G* employs eight-noded serendipity interpolation of displacements and 2×2 Gauss integration. The matrix $\mathbf{K}_{aa}$ possesses one zero-energy mode that disappears in an assembly of elements. With the matrix $\mathbf{K}^e_{\lambda\lambda}$ described above, this element shows proper convergence to a state with $F_{ip} \to 0$ and vanishing stress oscillations and is the most reliable of C^1-elements.

Element *R*34_*G* employs bi-quadratic lagrangian interpolation of displacements and 2×2 numerical integration. The element shows excellent behaviour, but only in sufficiently constrained configurations, since the matrix $\mathbf{K}_{aa}$ possesses three zero-energy modes, two of which propagate in an assembly of elements. With 3×3 integration the rank of $\mathbf{K}_{aa}$ is correct and in an assembly no extra boundary conditions for λ are necessary. However, these sampling points are not optimal for our problem (cf. the description of element *L*7*G*), mapping of stresses to the inside of the yield surface takes place at some Gauss points and convergence is gradually lost. Selective (3×3/2×2) integration of matrices $\mathbf{K}_{aa}$ and $\mathbf{K}_{\lambda\lambda}$ is not easily achieved because of the presence of the coupling matrices $\mathbf{K}_{\lambda a}$ in eq. (6.40). To preserve the optimal integration scheme for the yield condition and remove zero-energy deformation modes from element *R*34_*G*, hourglass control techniques could be used (cf. [19,20]), but the addition of a stabilization matrix to $\mathbf{K}_{aa}$ affects the consistency

of linearization and the presence of incompatible modes affects the accuracy of the return mapping, which leads to convergence deterioration.

Figure 6.5 shows three quadrilateral penalty-enhanced C^0-continuous elements with linear, quadratic serendipity and quadratic lagrange interpolation functions for the unknowns. The elements are formulated in a Cartesian global reference system, but they can be transformed. As is the case for the one-dimensional C^0-elements the nonsymmetric and symmetric formulation both yield convergent results.

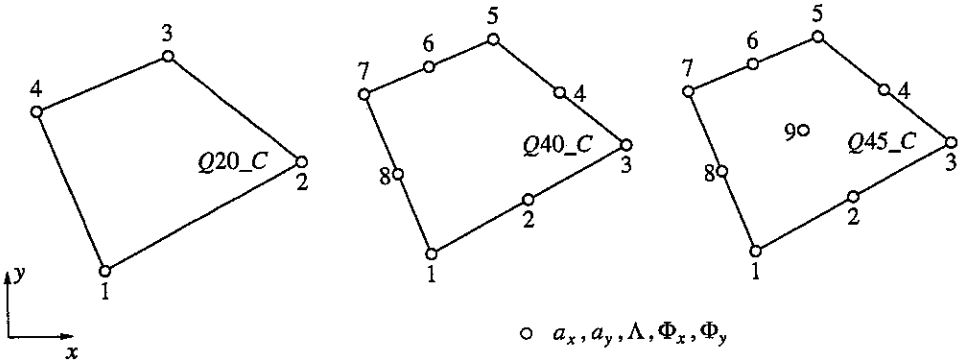

Figure 6.5 Quadrilateral penalty-enhanced C^0-elements.

All shape functions for element $Q20\_C$ are linear. Because of the penalty constraint this element can yield proper convergence only if one-point integration is used. With 2×2 Gauss integration the element locks: no zero eigenvalues exist in $\mathbf{K}^e_{\lambda\lambda}$, the constraint $\varphi_x = \lambda_{,x}$ is true everywhere and as a result the Laplacian is zero. However, a large number of spurious modes are present if one-point integration is employed: 2 hourglass modes for the displacement field $\mathbf{u}$ and 9 spurious modes for the λ field unless extra boundary conditions are introduced. The hourglass modes can be controlled, but, again, the anti-hourglass stiffness interferes with the gradient plasticity algorithm. No satisfactory way of controlling the spurious modes for λ has been found and the number of available boundary conditions is in general insufficient.

The quadratic lagrange element $Q45\_C$ with 2×2 integration converges perfectly. However, element $Q45\_C$ possesses zero-energy modes for $\mathbf{u}$ and also spurious modes for λ. In an arbitrary mesh the boundary conditions for ϕ_x or ϕ_y are not sufficient to assure the correct rank of the $\mathbf{K}^e_{\lambda\lambda}$ matrix and additional conditions for λ itself on part of the boundary are necessary to obtain a correct solution.

The quadratic serendipity element $Q40\_C$ with 2×2 integration does not converge very well, since the return mapping in eq. (6.76) is inaccurate for this element. Apparently the quadratic terms missing in the serendipity interpolation are important for interpolation compatibility. Since an assembly of elements $Q40\_C$ does not possess hourglass deformation modes, a combination of 8-noded interpolation of displacements and 9-noded interpolation of the λ and $\boldsymbol{\phi}$ fields is suggested and gives rise to element $Q43\_C$, quite similar to the 'heterosis' plate bending elements (cf. [21]). This element converges better and is a C^0 equivalent of the eight-noded element $R32\_G$.

6.6.3 Triangular elements

For a triangular element geometry the problem of choosing well-balanced interpolations of displacements and plastic multiplier as well as an optimal integration scheme becomes even more difficult. Experience with rectangles suggests the use of the lowest possible interpolation order and reduced integration. Figure 6.6 shows two triangular elements, which have a quadratic interpolation of displacements. The elements are formulated in area coordinates and, to avoid transformations, are referred to the global axes.

Element $T21\_G$ has a cubic interpolation of λ based on a non-conforming plate bending triangle [21]. The element does not fulfil the continuity requirements for λ_n on its boundary and is included in the present group because of the presence of Λ_x and Λ_y degrees of freedom. Integration with three Gauss points is used, as well as 3-point Hammer integration at the midsides of the triangle. Neither of these integration schemes are optimal: stresses are mapped inside the yield surface and stress oscillations are found. Additional boundary conditions for the plastic multiplier field are necessary to prevent the existence of non-zero λ modes in the elastic elements.

Element $T30\_G$ employs the shape functions derived in [22] and is fully C^1-compatible, has a quintic interpolation of λ and cubic distribution of λ_n along the sides. To prevent spurious λ modes 6 integration points and extra boundary conditions, involving Λ_n or Λ, and sometimes also second-order derivatives of the plastic multiplier are necessary.

It seems that for the above elements it is not possible to find sampling points, in which higher order accuracy of stress approximation and convergence of F_{ip} to zero is obtained. Consequently neither of them exhibits a fast convergence and stress oscillations are observed that may lead to violation of the positive yield strength condition and sometimes also to local unloading. Nevertheless, in numerical tests they give reasonable predictions of the global response and shear banding.

It is also difficult to construct C^0-continuous triangular elements which satisfy the requirements for interpolation and numerical integration mentioned in Section 6.3. We have limited our research to a low order interpolation. Figure 6.7 shows the three tested elements. The elements are formulated in area coordinates and referred to the global axes.

Element $T15\_C$ has a linear interpolation of all fields and uses one-point integration. The element has too many constraints in both standard and crossed diagonal meshes and does not converge.

Element $T30\_C$ has a uniform quadratic interpolation and is integrated using 3 Gauss points. Although full convergence is not achieved - mapping of stresses to the inside of the yield surface is observed and stress oscillations are found - this element gives acceptable results. In constrained configurations the use of one-point integration yields fast convergence and three integration points may cause locking.

In an arbitrary configuration the tangent operator determined using only one Gauss point is strongly rank-deficient and a solution cannot be obtained. This suggests the implementation of element $T24\_C$, with a linear interpolation of displacements and quadratic shape functions for the other fields, to be used with one-point

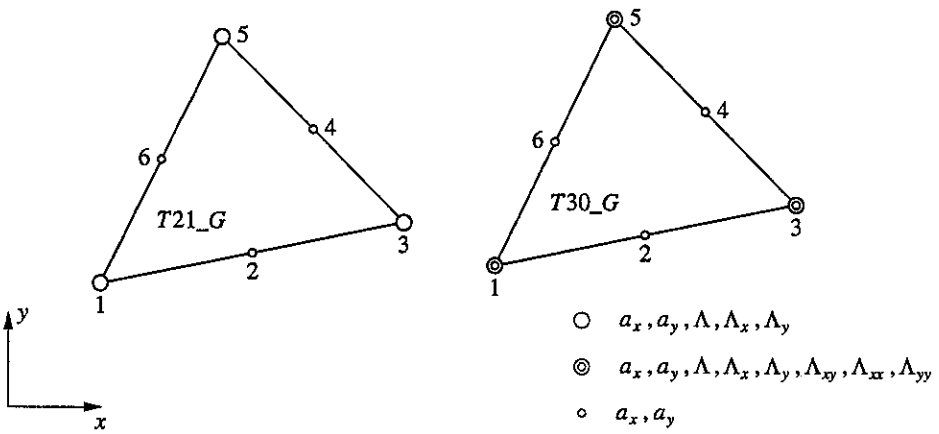

Figure 6.6 Triangular C^1-elements.

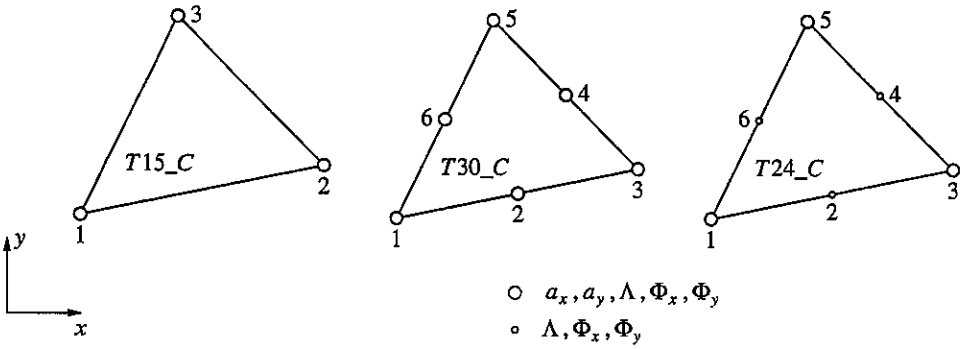

Figure 6.7 Triangular penalty-enhanced C^0-elements.

integration. However, this element shows an acceptable performance only in strongly constrained configurations, but fails otherwise as the previous one.

6.7 LOCALIZATION ANALYSES USING GRADIENT PLASTICITY

6.7.1 One-dimensional elements

Next we will present some results of one-dimensional and two-dimensional localization tests to demonstrate that the present formulation removes the spurious mesh sensitivity of finite element simulations. We will also compare the performance of the formulated gradient plasticity elements. We will limit our consideration to associated, gradient-enhanced J_2-plasticity (for other criteria, see [23]):

$$F = \sqrt{3J_2} - \bar{\sigma}(\kappa, \nabla^2\kappa) , \tag{6.79}$$

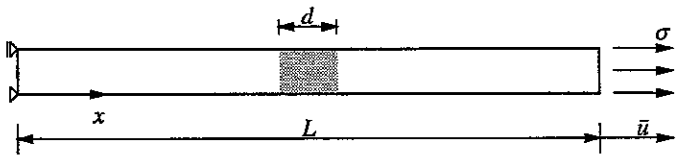

Figure 6.8 Imperfect bar in pure tension.

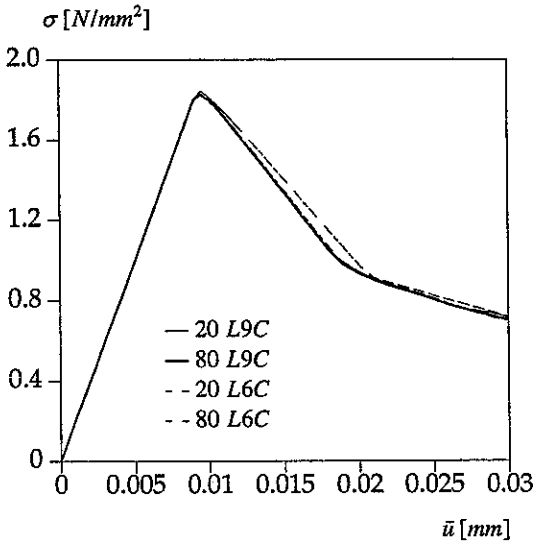

Figure 6.9 Load-displacement diagrams for C^0 one-dimensional elements.

where J_2 is the second invariant of the deviatoric stress tensor and $\bar{\sigma}$ is the yield strength.

We will first analyze an imperfect bar in tension, see Figure 6.8 [10]. For this one-dimensional problem the following simple yield function holds:

$$F = \sigma - \bar{\sigma}(\kappa) + g\,\frac{\mathrm{d}^2\kappa}{\mathrm{d}x^2}\,, \tag{6.80}$$

with σ the axial stress. The hardening parameter κ is now equal to the plastic multiplier λ and the axial plastic strain ε^{p}. According to the analytical solution derived in [10] the width of the localization zone w is given by:

$$w = 2\pi l\,, \tag{6.81}$$

with l the internal length scale defined as

$$l = \sqrt{-\frac{g}{h}}\,. \tag{6.82}$$

In eq. (6.82) $h = \mathrm{d}\bar{\sigma}/\mathrm{d}\varepsilon^{\mathrm{p}}$ is the hardening/softening modulus.

The following data are used in the numerical calculations: length of the bar

$L = 100\,mm$, Young's modulus $E = 20,000\,N/mm^2$, tensile strength $\sigma_y = 2\,N/mm^2$. The one-dimensional elements described in Sections 6.3 and 6.4 have been used. Two meshes of 20 and 80 elements have been used to examine the mesh-dependence of results. The elements in the middle of the bar ($d = 10\,mm$) have a 10% smaller value of σ_y. The derivative of the plastic multiplier is set to zero at both ends of the bar. Linear softening has been used with the softening modulus $h = -0.1\,E$. An internal length $l = 5\,mm$ is assumed, yielding $g = -l^2 h = 50,000\,N$. The corresponding width of the localization zone is $w = 31.4\,mm$.

We begin the comparison with C^0-continuous penalty-enhanced elements. The left diagram in Figure 6.9 shows load-displacement paths obtained using elements *L6C* and *L9C* with the (optimal) one-point and two-point Gauss integration, respectively. Immediate convergence has been observed in the calculations. While the coarse mesh with 20 linear elements *L6C* gives a slightly too stiff response and a disturbed λ distribution (Figure 6.10), the fine mesh and both meshes for the quadratic *L9C* element yield identical results. When all the inelastic points are in the softening regime, the slope of the load-displacement diagram is equal to the analytical value derived in [10]. The calculations are also stable when the strain in the centre elements exits the softening branch ($\kappa > \kappa_u$). The load-displacement diagrams then bend upwards and the localization zone broadens. This behaviour is a result of the fact that, when the softening modulus h goes to zero, while g is kept

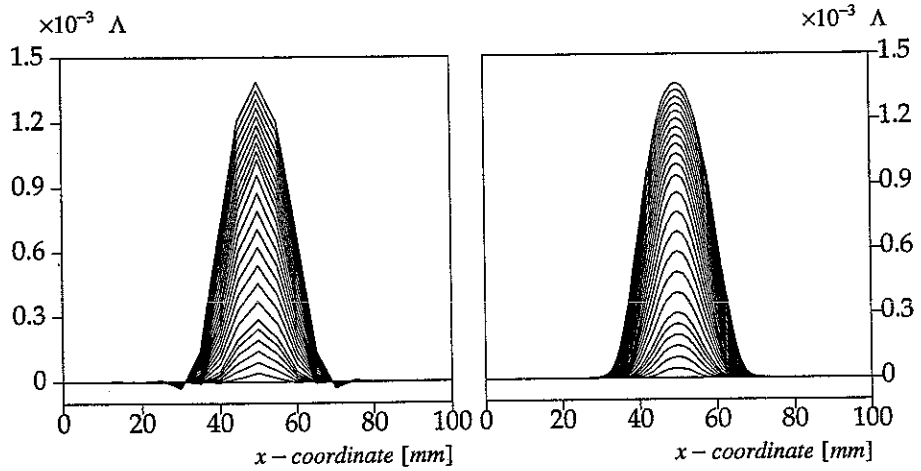

Figure 6.10 Evolution of the plastic strain distribution in the bar for 20 (left) and 80 (right) elements *L6C*.

constant, the internal length l locally increases to infinity.

Next, we apply the C^1-continuous elements *L7G* with quadratic interpolation of the displacement and hermitian interpolation of the plastic multiplier. Two different values of the internal length l are assumed: $l = 5\,mm$ (giving $g = 50,000\,N$ and $w = 31.4\,mm$) and $l = 2.5\,mm$ ($g = 12,500\,N$ and $w = 15.7\,mm$). Figure 6.11 shows the load-displacement diagrams for these cases. As long as all the points in the structure remain in the softening regime, the results for the two meshes with 20

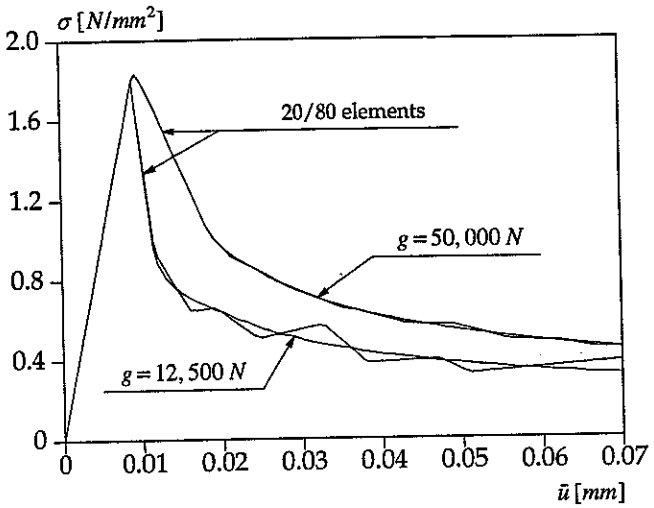

Figure 6.11 Mesh-sensitivity of load-displacement diagrams (elements *L7G*).

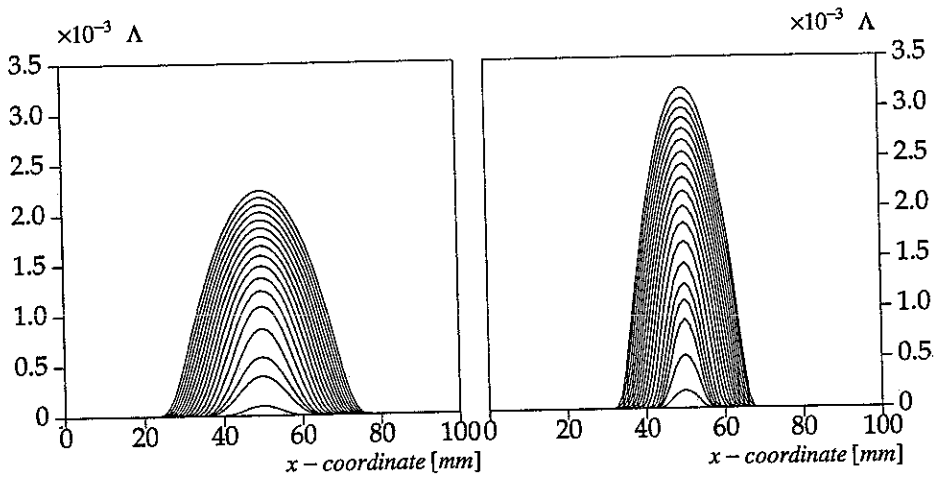

Figure 6.12 Evolution of plastic strains for $g = 50,000\ N$ (left) and $g = 12,500\ N$ (right).

and 80 elements are practically the same, and equal to those for the C^0-elements. This is not the case for the linear-hermitian element *L6G* [10], for which the orders of interpolation are not balanced properly. When in the centre points the softening branch is exited the calculations are stable, if a dense enough discretization is used. In Figure 6.11 the results for both meshes are similar for the larger regularization coefficient $g = 50,000\ N$, but for $g = 12,500\ N$ and for the coarse mesh oscillations are observed.

The comparison of the two diagrams in Figure 6.12 shows that the internal

length l governs the width of localization zone in the linear softening regime. When for an increasing number of Gauss points h equals zero, the width of the localization zone increases (Figure 6.12).

6.7.2 Quadrilateral elements

To demonstrate the potential of two-dimensional elements we consider a biaxially compressed specimen, in which strain localization into a shear band takes place at the onset of softening. The dimensions of the specimen are $B=60\,mm$ and $H=120\,mm$. The specimen is placed on a smooth rigid plane and its upper edge is constrained to remain horizontal while a vertical deformation equivalent to a compressive force is applied. The following parameter values are adopted: elastic shear modulus $G=4000\,N/mm^2$ and Poisson's ratio $\nu=0.49$. The gradient-dependent Huber-Mises yield function is adopted with an initial yield strength $\sigma_y=100\,N/mm^2$, a constant softening modulus $h=-0.1\,G$ and a gradient constant $g=3600\,N$, which corresponds to an internal length scale $l=3\,mm$ for pure shear. In the present calculations an imperfect zone with a 10% reduction of σ_y is introduced in the bottom left-hand corner of the specimen.

For C^1-elements extra boundary conditions for λ ($\Lambda_n=0$ and $\Lambda_{xy}=0$) are introduced on the whole circumference of the specimen. For the most reliable element $R32EG$ fast convergence is observed during the entire analysis, also when the yield strength in the most heavily strained elements goes to zero. The response is practically insensitive to mesh refinement (left part of Figure 6.13). Element $R34EG$ shows an even faster convergence and results for the coarse mesh are better, but the solution is spoiled by spurious hourglass deformation modes. The four-noded element $R24EG$ gives stiffer results (right part of Figure 6.13), but shows good convergence in spite of a poor match between the interpolations.

A performance similar to that of the $R34EG$ element is found for element $Q45EC$. However, for this element, the available boundary conditions for Φ_x and Φ_y are not sufficient to assure the correct rank of the $\mathbf{K}^e_{\lambda\lambda}$ matrix, negative pivots are found and spurious modes are observed for the plastic multiplier field. They can be prevented by setting the $\boldsymbol{\Lambda}$ degrees of freedom to zero on the upper edge of the model. The results are then similar to the two previous elements. Similar convergence and results are also exhibited by the 'heterosis' element $Q43EC$, where the spurious modes must be prevented only for the λ field. Stiffer results and poor convergence are found for element $Q45EC$ with 3×3 numerical integration, which supplies a sufficient rank of the matrices in elastic elements and prevents zero-energy modes, but introduces too many internal constraints and destroys the satisfaction of the yield condition, since optimal sampling points are not used. Element $Q20EC$ with 2×2 integration locks and shows no localization. The eight-noded element $Q40EC$ with 2×2 integration gives an acceptable load-deformation response, but, quite unexpectedly, does not converge well.

Figure 6.14 presents the deformation patterns obtained using element $R32EG$. Figure 6.15 presents contour lines of equal plastic multiplier values. Both figures show about the same width of the shear band for the three used meshes, especially

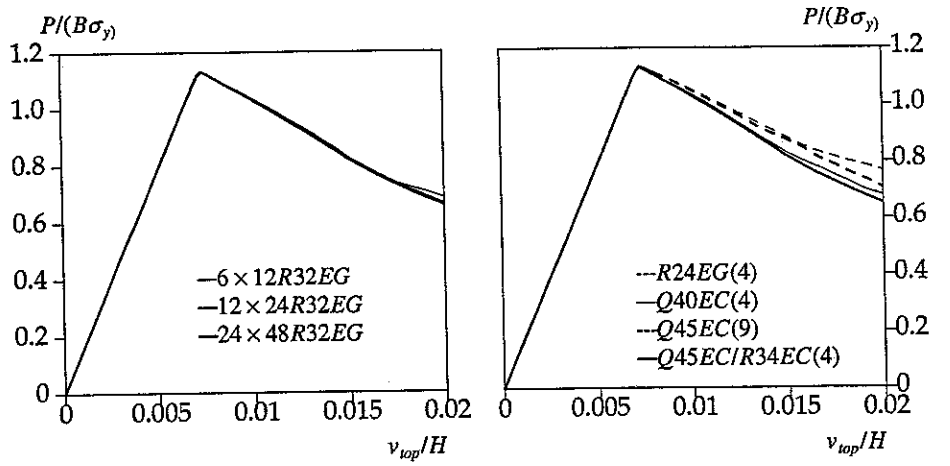

Figure 6.13 Load-displacement diagrams for three discretizations using element *R32EG* with 2×2 integration (left) and comparison of different elements with integration scheme given in brackets (right).

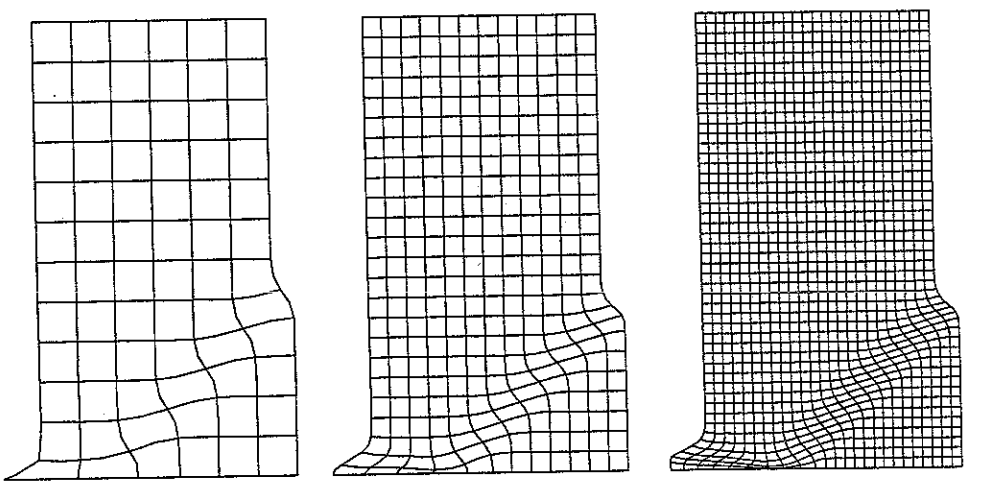

Figure 6.14 Deformation patterns for three discretizations ($R32EG$, $v_{top}/H = 0.02$).

for the medium and fine meshes. Figure 6.16 shows the evolution of the equivalent plastic strain field along the vertical symmetry axis of the specimen. For the coarse mesh spurious negative values of λ are visible next to the localization band. For the finer meshes λ profiles are similar to each other and smooth as expected.

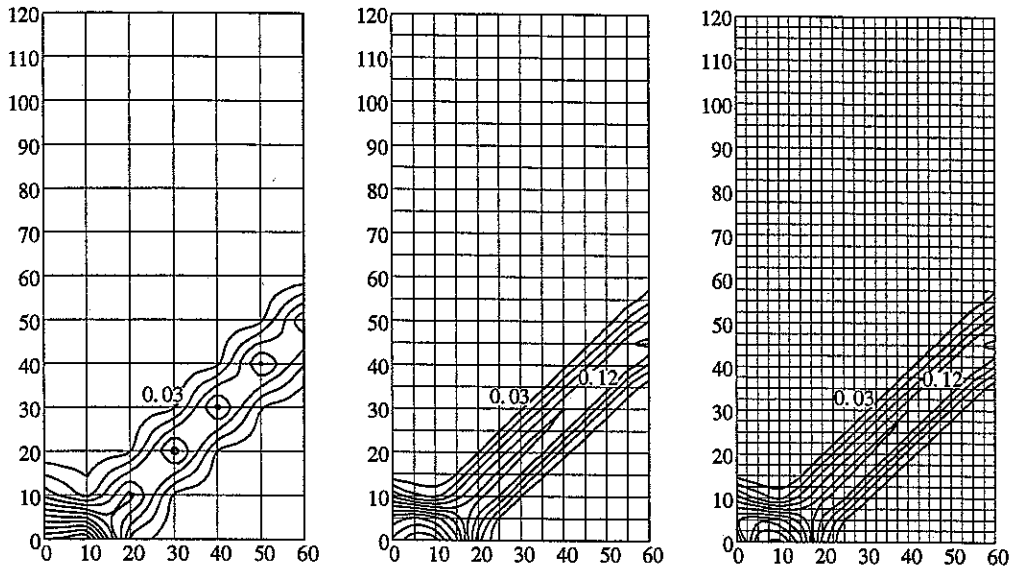

Figure 6.15 Contour plots of equivalent plastic strain ($R32EG$, $v_{top}/H = 0.02$).

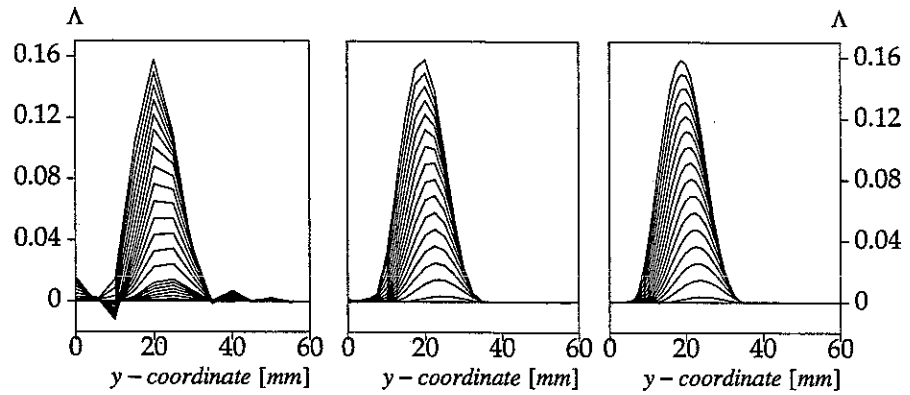

Figure 6.16 Evolution of the equivalent plastic strain along the vertical symmetry axis $x = 0$ (from the left: coarse, medium and fine mesh, elements $Q45EC$).

6.7.3 Triangular elements

The same biaxial compression test has been analyzed using three six-noded triangular elements: the C^1-element $T30EG$, the non-conforming element $T21EG$ and the C^0 penalty-enhanced element $T30EC$. Attention has been focused on the comparison of their sensitivity to mesh alignment. Figure 6.17 shows the load-displacement diagrams obtained for the discretization 12×24×4 (crossed diagonal) and 12×24×2

(with directional bias, i.e. with the elements aligned perpendicularly to the expected direction of a shear band). For element $T21EG$ 3 integration points and boundary conditions $\Lambda_n = 0$ are used (the solution without the boundary conditions is similar, but exhibits a few negative pivots). For element $T30EG$ 6 integration points and boundary conditions as for the previous element are employed (if additionally $\Lambda_{xy} = 0$ on the specimen edges, results are similar). For element $T30EC$ 3 integration points and boundary conditions for Φ_n (normal to the boundary) are used.

Despite the fact that none of the analyzed triangular elements ensures fast and full convergence, because the used integration stations are not Barlow points, for crossed-diagonal meshes all of them give a similar inclination of the post-peak equilibrium path and prediction of the shear band width and position (see Figure 6.18).

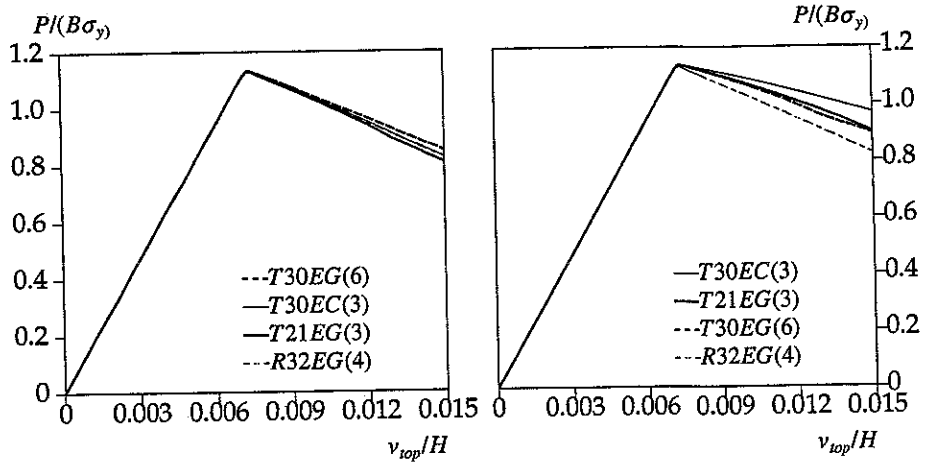

Figure 6.17 Comparison of the behaviour of C^1 and C^0 continuous triangular elements in crossed diagonal meshes (left) and in biased meshes (right).

The results are close to the results of element $R32EG$.

Figure 6.19 presents the deformation patterns obtained for the biased meshes. Although the shear bands extend from the weaker spot in the bottom left-hand corner of the specimen, the biased mesh makes the response stiffer, especially for the C^0-element $T30EC$, which also predicts a too broad shear band. For the C^1-elements the results are acceptable and the slight mesh alignment sensitivity is expected to vanish upon further mesh refinement.

6.8 WAVE DISPERSION IN A GRADIENT-DEPENDENT MEDIUM

We continue with a discussion on wave propagation in gradient plasticity and the effects of temporal and spatial discretization. In particular, we shall discuss the numerical dispersion introduced by the discretization, which adds to the already existing physical dispersion in gradient-dependent media.

We consider the one-dimensional bar of Figure 6.7, now loaded by an impact

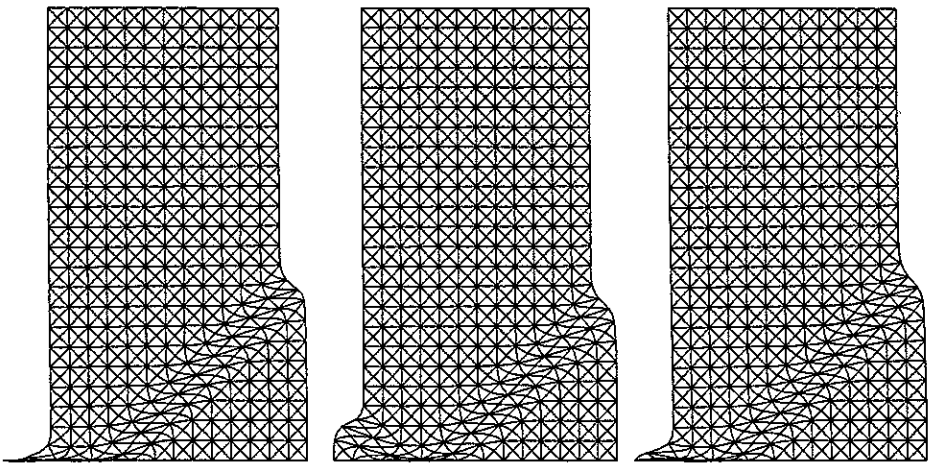

Figure 6.18 Deformation patterns for the crossed diagonal meshes 12×24×4 ($T21EG$ on the left, $T30EG$ in the middle, $T30EC$ on the right).

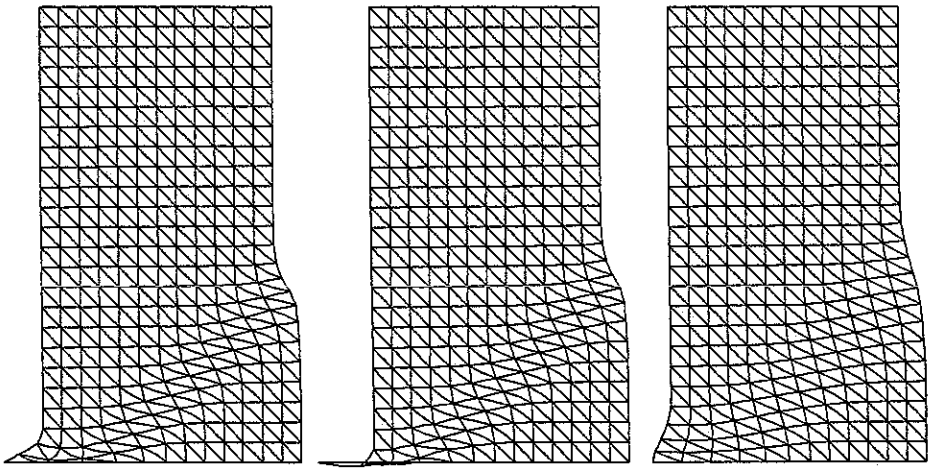

Figure 6.19 Sensitivity to mesh alignment exhibited by the triangular elements ($T21EG$ on the left, $T30EG$ in the middle, $T30EC$ on the right).

load. In this dynamic context the governing equations for motion and continuity read

$$\frac{\partial \sigma}{\partial x} = \rho \frac{\partial^2 u}{\partial t^2} \tag{6.83}$$

and

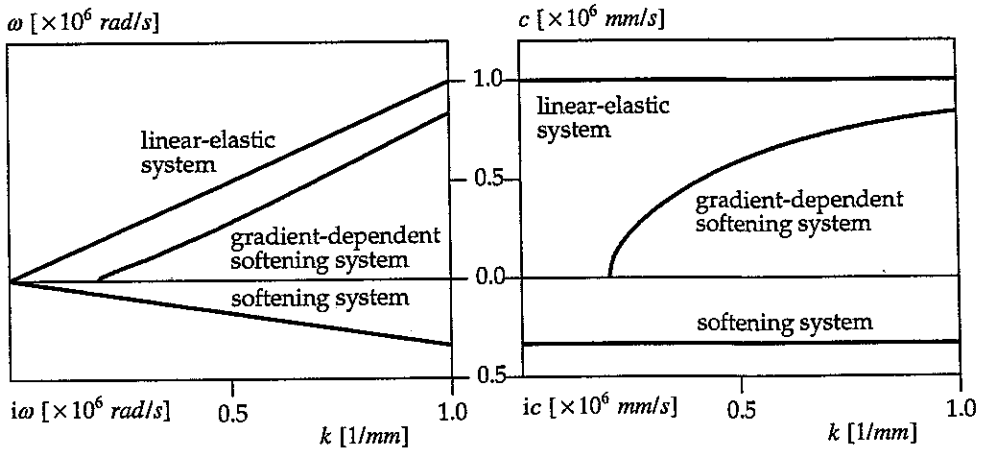

Figure 6.20 Continuum dispersion curves for linear-elastic, standard softening and gradient-dependent softening system. Left: Frequency versus wave number. Right: Phase velocity versus wave number.

$$\varepsilon = \frac{\partial u}{\partial x} , \tag{6.84}$$

with ρ the mass density, u the axial displacement, σ and ε stress and strain and x and t spatial and temporal variables, respectively. With the strain decomposition

$$\varepsilon = \varepsilon^{\mathrm{e}} + \varepsilon^{\mathrm{p}} , \tag{6.85}$$

and the bijective relation between stress σ and elastic strain ε^{e}

$$\sigma = E\varepsilon^{\mathrm{e}} , \tag{6.86}$$

the wave equation for one-dimensional gradient-dependent softening plasticity is derived as

$$\frac{g}{h+E}\left(E\frac{\partial^4 u}{\partial x^4} - \rho\frac{\partial^4 u}{\partial x^2 \partial t^2}\right) + \rho\frac{\partial^2 u}{\partial t^2} - \frac{hE}{h+E}\frac{\partial^2 u}{\partial x^2} = 0 . \tag{6.87}$$

For a dispersion analysis we consider a single harmonic wave which propagates through a one-dimensional element

$$u(x,t) = A\mathrm{e}^{\mathrm{i}(kx-\omega t)} . \tag{6.88}$$

The frequency ω is a function of the wave number k

$$\omega = f(k) , \tag{6.89}$$

and the function $f(k)$ is determined by the particular system under consideration. A system is considered to be dispersive if [24]

$$f''(k) \neq 0 , \tag{6.90}$$

in which a prime denotes differentiation with respect to k. In this case, the phase speed

$$c = \frac{\omega}{k} \tag{6.91}$$

is not the same for every wave number k and modes represented by its wave number travel at different speeds and will therefore disperse. Finally, we adopt the standard definitions for the wave length

$$\lambda = \frac{2\pi}{k} \tag{6.92}$$

and the period

$$T = \frac{2\pi}{\omega} \,. \tag{6.93}$$

We substitute the harmonic wave solution (6.88) into eq. (6.87). The dispersion relation for the gradient-dependent softening plasticity system is then elaborated as

$$\omega = c_e k \sqrt{\frac{h + gk^2}{E + h + gk^2}} \tag{6.94}$$

with $c_e = \sqrt{E/\rho}$ the so-called bar wave velocity. Now, the frequency is a real function of wave number k if

$$k \geq \sqrt{-\frac{h}{g}} \tag{6.95}$$

or using eq. (6.92)

$$\lambda \leq 2\pi\, l \,, \tag{6.96}$$

with l the internal length scale defined in eq. (6.82). Eq. (6.96) states that there exists a cut-off value for k. This value of k corresponds to the mode with the largest wave length that the gradient-dependent softening system can transmit. Above this value for k all frequencies are real.

Eq. (6.94) shows that for a non-zero gradient constant g, $f''(k) \neq 0$, so that wave propagation in the gradient-dependent plasticity system is dispersive. The dispersion curves have been plotted in Figure 6.20 for a linear-elastic system ($\omega = c_e k$), a standard softening plasticity system (with imaginary frequencies $\omega = ic_e k\sqrt{-h/(E+h)}$), and the gradient-dependent softening plasticity system. In the right part of Figure 6.20 the corresponding phase velocity - wave number ($c - k$) curve is shown. In Figures 6.20 the bar wave velocity $c_e = 1000\ m/s$, the Young's modulus $E = 20,000\ N/mm^2$, the softening modulus $h = -0.1E$ and the gradient constant $g = 50,000\ N$. The values for h and g imply a length scale parameter $l = 5.0\ mm$.

Dispersion in a softening system is closely related to the problem of localization of deformation. As a result of softening localization of deformation may occur and the behavior of localized zones is very much dependent on the dispersive

characteristics of the material [25-27]. For a standard softening plasticity system the inability of the material to transmit waves with a real frequency (and phase velocity) causes the strains to localize in zones of zero thickness. However, the dispersion contribution due to spatial discretization causes the frequency to reach a real zero value, and numerically a stationary wave with frequency and phase velocity equal to zero is computed in the localization zone [25]. The solution is now mesh dependent and corresponds to this stationary wave. Its wave length λ is equal to the width of the zone, namely a one finite element wide zone (for constant strain elements).

For the gradient-dependent softening system the fact that waves with real phase velocities disperse has the advantageous consequence that the localization zone can extend and that the strain profile in the localization zone can be transformed because different modes travel at different speeds. These features are of pivotal importance for simulating zones of localized deformation with a finite size instead of the zero-thickness solution as obtained for the softening plasticity system. Also for the gradient model the localization zone acts as a stationary wave with frequency and phase velocity equal to zero. For this reason the width of the localization zone w is equal to the lowest-order wave that the gradient-dependent softening system can transmit, i.e. $w = 2\pi l$. The width of the localization zone apppears as a consequence of the length scale effect and the spurious mesh dependence is removed [26].

In finite element formulations the governing equation for one-dimensional gradient-dependent softening plasticity (6.87) is discretized with respect to spatial and temporal variables. Discretization is another source of dispersion [27,28] and is introduced irrespective of the fact whether the underlying material exhibits dispersion of waves (gradient-dependent softening system) or not (standard softening system). The dispersion contribution of temporal and spatial discretization on a one-dimensional gradient-dependent plasticity system will be assessed next.

6.8.1 Dispersion contribution by temporal discretization

A general family of time integration algorithms is considered that contains the Hilber-Hughes-Taylor α-method [29] as well as the Newmark-method family [11]

$$\mathbf{M}\ddot{\mathbf{a}}^{t+\Delta t} + (1+\alpha)\mathbf{K}\mathbf{a}^{t+\Delta t} - \alpha\mathbf{K}\mathbf{a}^{t} = 0\,, \tag{6.97}$$

$$\mathbf{a}^{t+\Delta t} = \mathbf{a}^{t} + \Delta t\dot{\mathbf{a}}^{t} + \Delta t^2[(1/2 - \beta)\ddot{\mathbf{a}}^{t} + \beta\ddot{\mathbf{a}}^{t+\Delta t}]\,, \tag{6.98}$$

$$\dot{\mathbf{a}}^{t+\Delta t} = \dot{\mathbf{a}}^{t} + \Delta t[(1-\gamma)\ddot{\mathbf{a}}^{t} + \gamma\ddot{\mathbf{a}}^{t+\Delta t}]\,, \tag{6.99}$$

with $\ddot{\mathbf{a}}$, $\dot{\mathbf{a}}$ and $\mathbf{a}$ the nodal accelerations, velocities and displacements, respectively. Eqs. (6.97)-(6.99) represent a semi-discrete system with mass matrix $\mathbf{M}$ and stiffness matrix $\mathbf{K}$, which is assumed to be constant over Δt. In this section spatial discretization is ignored and the continuum values for $\mathbf{M}$ and $\mathbf{K}$ will be substituted. The integration parameters α, β and γ determine the stability, accuracy and dissipative properties of the system. Moreover, these parameters have an influence on dispersion, which will be demonstrated in this paper for softening materials. Taking

$\alpha = 0$ the scheme reduces to the Newmark-method family with $\gamma = 1/2$ and $\beta = 1/4$ the average acceleration method, $\gamma = 1/2$ and $\beta = 1/12$ the Fox-Goodwin method and $\gamma = 1/2$ and $\beta = 0$ the central difference method. Numerical dissipation can be introduced when $\gamma > 1/2$. However, from linear-elastic considerations [11] it is known that second-order accuracy is then lost. For this reason the α-method was developed [29] in which numerical dissipation is introduced for $-1/3 < \alpha < 0$ while second-order accuracy can be preserved if $\gamma = 1/2 - \alpha$ and $\beta = 1/4(1 - \alpha)^2$.

A gradient-dependent softening system exhibits physical wave dispersion as well as numerical dispersion. By carrying out a dispersion analysis, the interaction between physical and numerical dispersion is now assessed. For the problem governed by eq. (6.87) a solution according to

$$u(x,t) = \bar{u}(t)e^{ikx} \tag{6.100}$$

is assumed. Substitution of this equation into eq. (6.87) eliminates the spatial derivative terms, and leads to

$$\rho \frac{\partial^2 \bar{u}}{\partial t^2} + \frac{Ek^2(gk^2 + h)}{gk^2 + h + E} \bar{u} = 0 . \tag{6.101}$$

Discrete nodal values are now substituted for the displacement function, i.e., $\bar{u}(t) = \mathbf{a}$, so that

$$M\ddot{\mathbf{a}} + K\mathbf{a} = \mathbf{0} , \tag{6.102}$$

with

$$M = \rho \tag{6.103}$$

$$K = \frac{Ek^2(gk^2 + h)}{gk^2 + h + E} . \tag{6.104}$$

By considering the set of equations (6.97)-(6.99) at $t-2\Delta t$, $t-\Delta t$, t and $t+\Delta t$ the time derivatives $\dot{a}^{t-\Delta t}$, $\dot{a}^t$, $\ddot{a}^{t-\Delta t}$, $\ddot{a}^t$ and $\ddot{a}^{t+\Delta t}$ can be eliminated and a temporally discretized equation of motion can be derived according to

$$K(c_0 a^{t+\Delta t} - c_1 a^t - c_2 a^{t-\Delta t} - c_3 a^{t-2\Delta t}) = \frac{M}{\Delta t^2}(-a^{t+\Delta t} + 2a^t - a^{t-\Delta t}) , \tag{6.105}$$

with

$$c_0 = \beta(1 + \alpha) , \tag{6.106}$$

$$c_1 = \beta\alpha + (1 + \alpha)(2\beta - \gamma - 1/2) \tag{6.107}$$

$$c_2 = (1 + \alpha)(\gamma - \beta - 1/2) - \alpha(2\beta - \gamma - 1/2) \tag{6.108}$$

$$c_3 = -\alpha(\gamma - \beta - 1/2) \tag{6.109}$$

Harmonic solutions are now assumed, as follows

$$a^t = Ae^{i\omega t} , \tag{6.110}$$

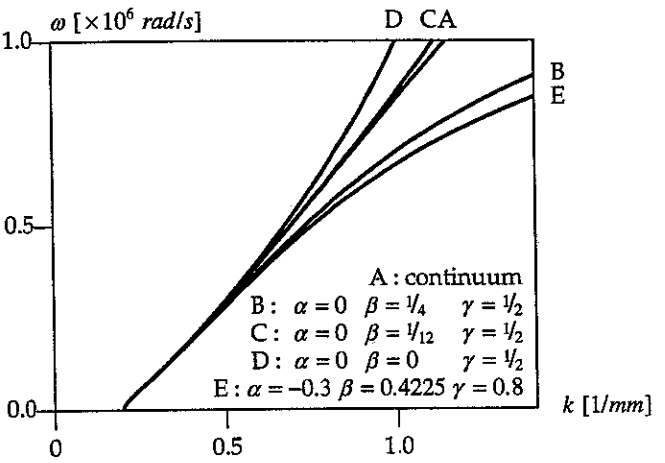

Figure 6.21 Dispersion curve for temporally discretized gradient-plasticity system. Variation of time integration scheme using $\Delta t = 2 \cdot 10^{-6}$ s.

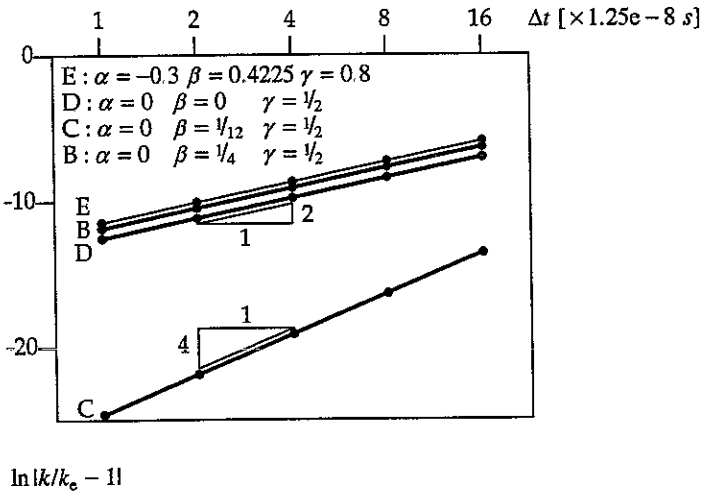

Figure 6.22 Convergence of time stepping schemes.

$$a^{t+\Delta t} = A e^{i\omega(t+\Delta t)} = A(\cos \omega \Delta t + i \sin \omega \Delta t) e^{i\omega t}, \tag{6.111}$$

$$a^{t-\Delta t} = A e^{i\omega(t-\Delta t)} = A(\cos \omega \Delta t - i \sin \omega \Delta t) e^{i\omega t}, \tag{6.112}$$

$$a^{t-2\Delta t} = A e^{i\omega(t-2\Delta t)} = A(\cos 2\omega \Delta t - i \sin 2\omega \Delta t) e^{i\omega t}, \tag{6.113}$$

which, after substitution into eq. (6.105), gives the dispersion relation with real and imaginary components. It appears that the real part offers the non-trivial solution by

$$k^2 = \tfrac{1}{2}\left(\frac{D_1}{c_e^2\Delta t^2} - \frac{hD_2}{g}\right) + \tfrac{1}{2}\left(\frac{D_1^2}{c_e^4\Delta t^4} + \frac{h^2D_2^2}{g^2} + \frac{2(2E+h)D_1D_2}{c_e^2\Delta t^2 g}\right)^{\frac{1}{2}}, \quad (6.114)$$

in which

$$D_1 = 2(1 - \cos\omega\Delta t)\,, \quad (6.115)$$

$$D_2 = (c_0 - c_2)\cos\omega\Delta t - c_3\cos 2\omega\Delta t - c_1\,, \quad (6.116)$$

and the real phase velocity follows from $c^2 = \omega^2 / k^2$.

In Figure 6.21 the dispersion curve has been plotted for different time integration schemes. The Fox-Goodwin method shows the best performance for gradient-dependent softening plasticity. It is remarkable that the Fox-Goodwin method, although the method is implicit on the basis of linear elastic considerations, gives an upper bound approximation of the continuum dispersion curve just like the central difference scheme. The average acceleration method and the α-method underestimate the frequency ω leading to elongated periods T. In Figure 6.22 the rate of convergence is plotted for the time integration schemes by means of the difference with the continuum solution at $k_e = 1.0\ 1/mm$. The results show that the Fox-Goodwin method exactly reaches $O(\Delta t^4)$ accuracy while the average acceleration method, the α-method and the central difference scheme perform $O(\Delta t^2)$ accurate.

Softening is the driving force for localization of deformation and the localization zone is represented by a stationary wave with frequency ω and phase velocity c both equal to zero. In Figures 6.21 and 6.23, in which the phase velocity is plotted against the wave number for the average acceleration scheme, the stationary wave is reflected by the cut-off value for wave number $k = \sqrt{-h/g}$. It appears that this value is not affected by the time integration scheme (Figure 6.21) or the time step (Figure 6.23).

6.8.2 Dispersion contribution by spatial discretization

To assess the effects of spatial discretization on the dispersive behaviour we consider the C^1-continuous two-noded bar element with two-point Gaussian quadrature ($L6G$) and we assume harmonic solutions of the form

$$u(x,t) = \bar{u}(x)\,e^{i\omega t}\,, \quad (6.117)$$

$$\varepsilon^p(x,t) = \bar{\varepsilon}^p\,e^{i\omega t}\,. \quad (6.118)$$

We now substitute eqs (6.117)-(6.118) into the weak forms of the equation of motion

$$-\rho\omega^2\int_L \delta\dot{\bar{u}}\cdot\dot{\bar{u}}\,dx + \int_L \delta\dot{\bar{\varepsilon}}\cdot E(\dot{\bar{\varepsilon}} - \dot{\bar{\varepsilon}}^p)\,dx = 0\,, \quad (6.119)$$

and the consistency condition

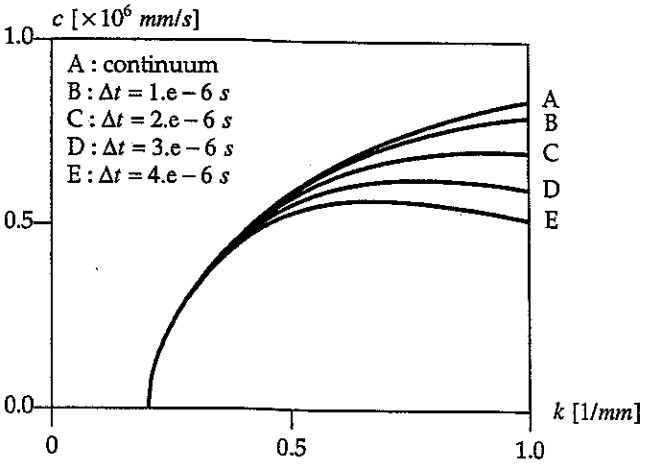

Figure 6.23 Influence on phase velocities of a variation of the time step for the average acceleration method.

$$\int_L \delta\dot{\bar{\varepsilon}}^p [E(\dot{\bar{\varepsilon}} - \dot{\bar{\varepsilon}}^p) - h\dot{\bar{\varepsilon}}^p + g\frac{\partial^2 \dot{\bar{\varepsilon}}^p}{\partial x^2}]\,dx = 0 \tag{6.120}$$

where the identity $\dot{\bar{\sigma}} = E(\dot{\bar{\varepsilon}} - \dot{\bar{\varepsilon}}^p)$ has been used. If we discretize $\bar{u}$, $\bar{\varepsilon}$, $\bar{\varepsilon}^p$ and $\partial^2\bar{\varepsilon}^p/\partial x^2$ according to eqs (6.33)-(6.35) and (6.38) we obtain

$$(\mathbf{K}_{aa} - \omega^2\mathbf{M}_{aa})\dot{\mathbf{a}} - \mathbf{K}_{a\lambda}\dot{\boldsymbol{\Lambda}} = \mathbf{0}\,, \tag{6.121}$$

$$\mathbf{K}_{\lambda a}\dot{\mathbf{a}} + \mathbf{K}_{\lambda\lambda}\dot{\boldsymbol{\Lambda}} = \mathbf{0}\,, \tag{6.122}$$

where

$$\mathbf{M}_{aa} = \rho\int_V \mathbf{H}^T\mathbf{H}\,dV \tag{6.123}$$

is the mass matrix, and the stiffness matrices $\mathbf{K}_{aa}$ and $\mathbf{K}_{a\lambda}$, and $\mathbf{K}_{\lambda a}$ and $\mathbf{K}_{\lambda\lambda}$ have been defined before (6.41)-(6.43). We assume a mesh with elements of constant length d and consider eqs (6.121) and (6.122) for node j, which results in the following three equations with the unknowns $\dot{a}$, $\dot{\Lambda}$ and $\dot{\Lambda}_x$

$$-\frac{\rho\omega^2 d}{16}(3\dot{a}_{j-1} + 10\dot{a}_j + 3\dot{a}_{j+1}) + \frac{E}{d}(-\dot{a}_{j-1} + 2\dot{a}_j - \dot{a}_{j+1}) -$$
$$\frac{E}{2}(\dot{\Lambda}_{j-1} - \dot{\Lambda}_{j+1}) - \frac{Ed}{32}(3\dot{\Lambda}_{x,j-1} - 6\dot{\Lambda}_{x,j} + 3\dot{\Lambda}_{x,j+1}) = 0\,, \tag{6.124}$$

$$\frac{E}{2}(-\dot{a}_{j-1}+\dot{a}_{j+1})-\frac{(h+E)d}{1024}(135\dot{\Lambda}_{j-1}+754\dot{\Lambda}_j+135\dot{\Lambda}_{j+1})-$$
$$\frac{(h+E)d^2}{2048}(63\dot{\Lambda}_{x,j-1}-63\dot{\Lambda}_{x,j+1})+$$
$$\frac{g}{32d}(33\dot{\Lambda}_{j-1}+66\dot{\Lambda}_j+33\dot{\Lambda}_{j+1})+\frac{g}{64}(\dot{\Lambda}_{x,j-1}-\dot{\Lambda}_{x,j+1})=0\,, \tag{6.125}$$
$$\frac{Ed}{32}(3\dot{a}_{j-1}-6\dot{a}_j+3\dot{a}_{j+1})-\frac{(h+E)d^2}{2048}(-63\dot{\Lambda}_{j-1}+63\dot{\Lambda}_{j+1})-$$
$$\frac{(h+E)d^3}{4096}(-27\dot{\Lambda}_{x,j-1}+90\dot{\Lambda}_{x,j}-27\dot{\Lambda}_{x,j+1})+$$
$$\frac{g}{64}(-9\dot{\Lambda}_{j-1}+9\dot{\Lambda}_{j+1})+\frac{gd}{128}(3\dot{\Lambda}_{x,j-1}-42\dot{\Lambda}_{x,j}+3\dot{\Lambda}_{x,j+1})=0\,, \tag{6.126}$$

in which a consistent mass matrix has been used. We can find a consistent set of harmonic solutions of the form

$$\dot{a}_j = A\mathrm{e}^{\mathrm{i}kx}\,, \tag{6.127}$$
$$\dot{\Lambda}_j = \mathrm{i}kB\mathrm{e}^{\mathrm{i}kx}\,, \tag{6.128}$$
$$\dot{\Lambda}_{x,j} = k^2C\mathrm{e}^{\mathrm{i}kx}\,. \tag{6.129}$$

The set of solutions at the neighbouring nodes $j\pm1$ is then

$$\dot{a}_{j\pm1} = A\mathrm{e}^{\mathrm{i}k(x\pm d)}\,, \tag{6.130}$$
$$\dot{\Lambda}_{j\pm1} = \mathrm{i}kB\mathrm{e}^{\mathrm{i}k(x\pm d)}\,, \tag{6.131}$$
$$\dot{\Lambda}_{x,j\pm1} = k^2C\mathrm{e}^{\mathrm{i}k(x\pm d)}\,. \tag{6.132}$$

Substitution of the complete solution (eqs (6.127)-(6.132)) in the spatially discretized equations of motion (6.124)-(6.126) gives a system of three equations for which the non-trivial solution reads

$$\omega = c_e\sqrt{\left(\frac{2}{d^2}+\frac{3k^2K_{d2}}{16}\right)\frac{(1-\cos kd)}{M_d}-\frac{kK_{d1}}{d}\frac{\sin kd}{M_d}}\,. \tag{6.133}$$

The parameter M_d is dependent on the mass distribution. For a consistent, a lumped and a higher-order mass matrix, respectively, we derive

$$M_d = \tfrac{1}{8}(5+3\cos kd)\,, \tag{6.134}$$
$$M_d = 1 \tag{6.135}$$
$$M_d = \tfrac{1}{16}(13+3\cos kd)\,. \tag{6.136}$$

The values K_{d1} and K_{d2} in eq. (6.133) are defined by

$$K_{d1} = E\left(\frac{D_4}{D_2}\sin kd-\frac{3d}{16}(\cos kd-1)\right)\left(\frac{D_2}{D_2D_3-D_1D_4}\right), \tag{6.137}$$

$$K_{d2} = -\frac{1}{D_2}\left(E \sin kd + D_1 K_{d1}\right), \tag{6.138}$$

with the functions

$$D_1 = k\left(\left(\frac{33g}{16d} - \frac{135(h+E)d}{512}\right)\cos kd - \frac{33g}{16d} - \frac{377(h+E)d}{512}\right), \tag{6.139}$$

$$D_2 = k^2\left(-\frac{g}{32} + \frac{63(h+E)d^2}{1024}\right)\sin kd\,, \tag{6.140}$$

$$D_3 = k\left(-\frac{9g}{32} + \frac{63(h+E)d^2}{1024}\right)\sin kd\,, \tag{6.141}$$

$$D_4 = k^2\left(\left(\frac{3gd}{64} + \frac{27(h+E)d^3}{2048}\right)\cos kd - \frac{21gd}{64} - \frac{45(h+E)d^3}{2048}\right). \tag{6.142}$$

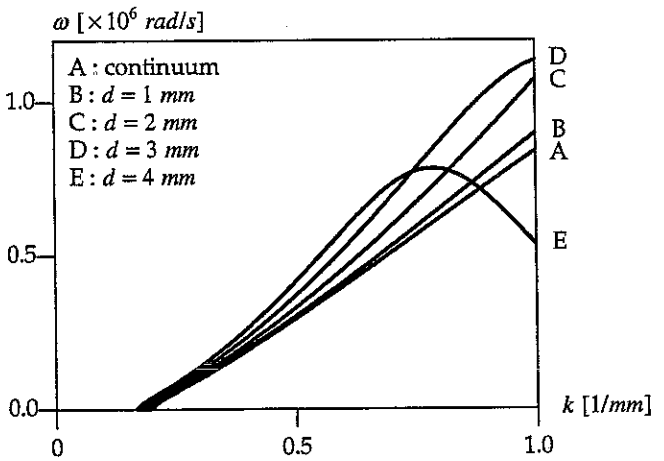

Figure 6.24 Influence of spatial discretization on the dispersion: Variation of element length d using a consistent mass matrix.

The dispersion curve of the discretized bar for a consistent mass distribution is plotted in Figure 6.24 for different sizes d of the finite element. We observe that refinement of the mesh ($d \to 0$) leads to convergence of the dispersion curve to the continuum dispersion curve. We obtain an upper bound estimate for the frequency using consistent mass distribution. The influence of the mass discretization is shown in Figure 6.25, in which a consistent, a lumped and a higher-order mass matrix have been used for a finite element with size $d = 2.0$ *mm*. The lumped mass matrix provides lower bound values, while the higher-order mass matrix leads to the best result. In Figure 6.26, where ω is calculated for $k = 1.0$ $1/mm$ by means of

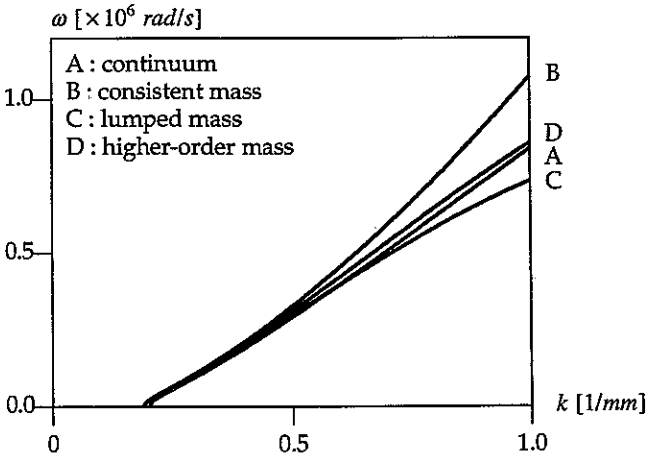

Figure 6.25 Influence of spatial discretization on the dispersion: Variation of the mass discretization using $d = 2\ mm$.

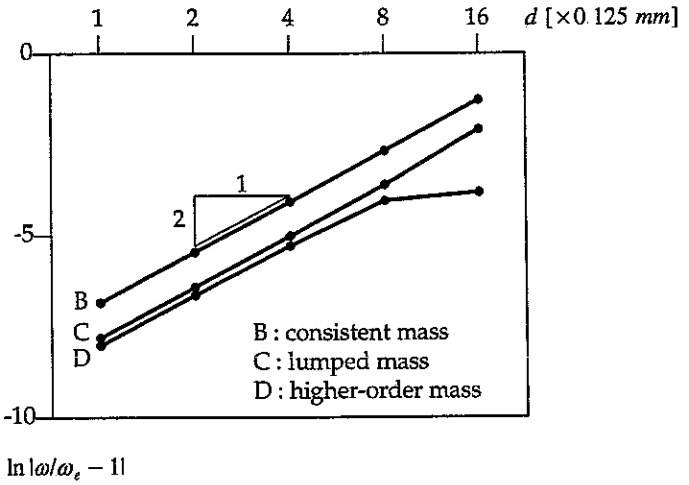

Figure 6.26 Convergence of mass discretization.

eqs (6.133)-(6.138) and ω_e is the exact frequency from the continuum dispersion analysis, we observe that the higher-order mass matrix gives the best results but does not increase the order of accuracy. So, a higher-order matrix in a gradient-dependent softening plasticity context does not imply a higher-order accuracy. Another result of the variation of mass matrices is that the type of distribution does not affect the width of a stationary localization zone. The cut-off value for wave number k and implicitly also for wave length λ is the same for the three curves in Figure 6.25. This result is logical since inertia effects do not play a role in a stationary localization zone.

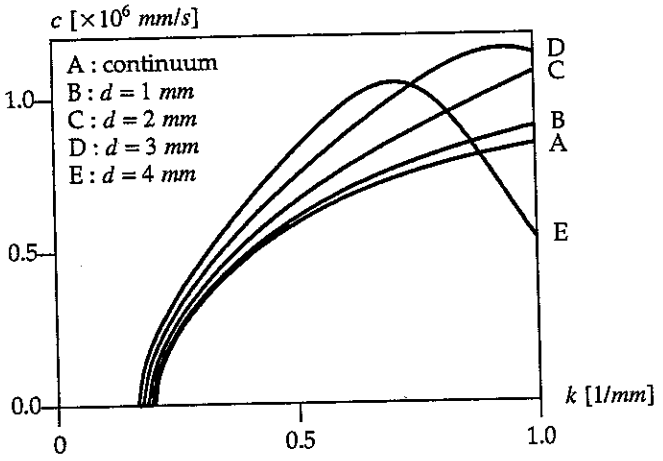

Figure 6.27 Dispersion curve for spatially discretized gradient-plasticity system - phase velocities as a function of the element size d using a consistent mass matrix.

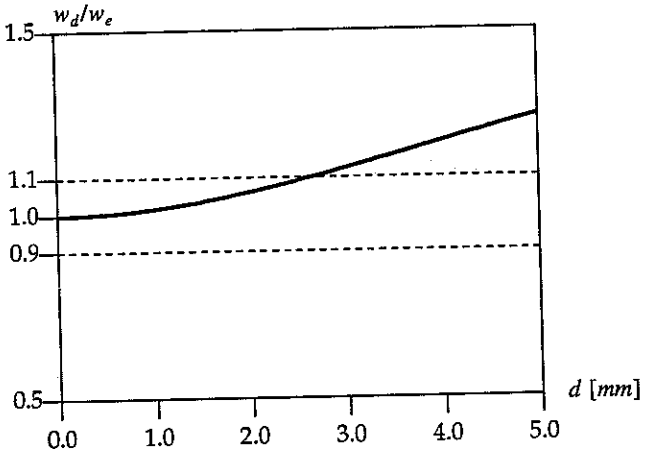

Figure 6.28 Influence of spatial discretization on the width of the localization zone.

An important observation from Figure 6.27, in which the phase velocity has been plotted against the wave number, is that the point that represents the stationary localization wave ($c = 0$) gradually moves to a smaller value of k when larger elements are used. This means that the wave length ($= 2\pi/k$), which represents the width of the localization zone, increases. This is exactly what is observed in numerical calculations with gradient-dependent softening plasticity models [26]. This widening of the localization band can be quantified exactly. If we take $c = 0$ in the discretized dispersion relation a dependence can be derived between the width of

the localization zone in the discretized continuum w_d and the element size d. This result is plotted in Figure 6.28, in which w_d is normalized with respect to the exact width of the localization zone $w_e = 2\pi l$. A criterion for the required number of finite elements n_{elem} in the localization zone can be derived. For instance, if a 10% mismatch between discretized and exact value is accepted it follows that the minimum number of finite elements is

$$n_{elem} \geq \frac{w_e}{d_{cri\pm 10\%}} = 11.8 \,. \tag{6.143}$$

It is noted that the C^1-continuous element with a quadratic interpolation for the velocity field ($L7G$) results in a much less severe condition. Eq. (6.143) is derived for a consistent mass distribution while temporal discretization effects were not considered. However, variation of the mass discretization (see Figure 6.25) and variation of the time integration scheme (Figure 6.21) confirm that the wave number of the cut-off mode (and therefore the width of the localization zone) was not affected and eq. (6.143) will not be different if all discretization influences would have been taken into account.

BIBLIOGRAPHY

[1] Aifantis, E.C. (1984) On the microstructural origin of certain inelastic models, *J. Engng. Mater. Technol.*, **106** , 326-334.

[2] Aifantis, E.C. (1987) The physics of plastic deformation, *Int. J. Plasticity*, **3** , 211-247.

[3] Aifantis, E.C. (1992) On the role of gradients in the localization of deformation and fracture, *Int. J. Engng. Sci.*, **30** , 1279-1299.

[4] Coleman, B. and Hodgdon, M.L. (1985) On shear bands in ductile materials, *Arch. Ration. Mech. Anal.*, **90** , 219-247.

[5] Lasry, D. and Belytschko, T. (1988) Localization limiters in transient problems, *Int. J. Solids Structures*, **24** , 581-597.

[6] Zbib, H.M. and Aifantis, E.C. (1988) On the localization and postlocalization behavior of plastic deformation, I,II,III, *Res Mechanica*, **23** , 261-277, 279-292, 293-305.

[7] Mühlhaus, H.-B. and Aifantis, E.C. (1991) A variational principle for gradient plasticity, *Int. J. Solids Structures*, **28** , 845-858.

[8] Schreyer, H.L. and Chen, Z. (1986) One-dimensional softening with localization, *ASME J. Appl. Mech.* **53** , 791-797.

[9] Vardoulakis, I. and Aifantis, E.C. (1991) A gradient flow theory of plasticity for granular materials, *Acta Mechanica*, **87** , 197-217.

[10] de Borst, R. and Mühlhaus, H.-B. (1992) Gradient-dependent plasticity: Formulation and algorithmic aspects, *Int. J. Num. Meth. Eng.*, **35** , 521-539.

[11] Hughes, T.J.R. (1987) *The Finite Element Method. Linear Static and Dynamic Finite Element Analysis.* Prentice-Hall, New Jersey.

[12] Pamin, J. and de Borst, R. (1994) Gradient plasticity and finite elements in the simulation of concrete fracture, *Proc. EURO-C 1994 Int. Conf. Computer Modelling of Concrete Structures*, Eds. H. Mang, N. Bićanić and R. de Borst,

Pineridge Press, Swansea, 393-402.

[13] Ortiz, M. and Morris, G.R. (1988) C^0 finite element discretization of Kirchhoff's equations of thin plate bending, *Int. J. Num. Meth. Eng.*, **26** , 1551-1566.

[14] Simo, J.C. and Taylor R.L. (1985) Consistent tangent operators for rate-independent elasto-plasticity, *Comp. Meth. Appl. Mech. Eng.*, **48** , 101-118.

[15] Runesson, K., Samuelsson, A. and Bernspang, L. (1986) Numerical technique in plasticity including solution advancement control, *Int. J. Num. Meth. Eng.*, **22** , 769-788.

[16] Ortiz, M. and Simo, J.C. (1986) An analysis of a new class of integration algorithms for elastoplastic constitutive relations, *Int. J. Num. Meth. Eng.*, **23** , 353-366.

[17] Barlow, J. (1976) Optimal stress locations in finite element model, *Int. J. Num. Meth. Eng.*, **10** , 243-251.

[18] Pamin, J. and de Borst, R. (1992) A rectangular element for gradient plasticity, *Proc. Third Int. Conf. Computational Plasticity: Fundamentals and Applications*, Eds D.R.J. Owen, E. Onate and E. Hinton, Pineridge Press, Swansea, 2009-2020.

[19] Wong, B.L. and Belytschko T. (1987) Assumed strain stabilization procedure for the 9-node Lagrange plane and plate elements, *Eng. Comput.*, **4** , 229-239.

[20] Liu, W.K., Ong, J.S.-J. and Uras, R.A. (1985), Finite element stabilization matrices - a unification approach, *Comp. Meth. Appl. Mech. Eng.*, **53** , 13-46.

[21] Zienkiewicz, O.C. and Taylor, R.L. (1991) *The Finite Element Method, Fourth edition*, Vol. 2, McGraw-Hill, London.

[22] Dasgupta, S. and Sengupta, D. (1990) A higher-order triangular plate bending element revisited, *Int. J. Num. Meth. Eng.*, **30** , 419-430.

[23] Pamin, J. (1994) *Gradient-Dependent Plasticity in Numerical Simulation of Localization Phenomena.* Dissertation, Delft University of Technology, Delft.

[24] Whitham, G.B. (1974) *Linear and Nonlinear Waves.* Wiley, London and New York.

[25] Sluys, L.J. (1992) *Wave Propagation, Localisation and Dispersion in Softening Solids.* Dissertation, Delft University of Technology, Delft.

[26] Sluys, L.J., de Borst, R. and Mühlhaus, H.-B. (1993) Wave propagation, localization and dispersion in a gradient-dependent medium, *Int. J. Solids Structures*, **30** , 1153-1171.

[27] Sluys, L.J. and de Borst, R. (1994) Dispersive properties of gradient-dependent and rate-dependent media, *Mechanics of Materials*, **18** , 131-149.

[28] Huerta, A. and Pijaudier-Cabot, G. (1994) Discretization influence on the regularization by two localization limiters, *ASCE J. Eng. Mech.* **120** , 1198-1218.

[29] Hilber, H.M., Hughes, T.J.R. and Taylor, R.L. (1977) Improved numerical dissipation for time integration algorithms in structural dynamics, *Earthquake Engng. and Structural Dynamics*, **5** , 283-292.